Dissipation and Bathymetric Sensitivities in an Unstructured Mesh Global Tidal Model

Coleman Blakely[1], Guoming Ling[1], William James Pringle[2], María Teresa Contreras[1], Damrongsak Wirasaet[1], Joannes Westerink[1], Saeed Moghimi[3], Greg Seroka[4], Lei Shi[5], Edward P. Myers III[6], Margaret Owensby[7], and Thomas Christopher Massey[8]

[1]University of Notre Dame
[2]Argonne National Laboratory
[3]NOAA/NOS
[4]NOAA/NOS Coast Survey Development Lab
[5]National Oceanic and Atmospheric Administration (NOAA)
[6]NOAA CSDL
[7]Coastal and Hydraulics Laboratory, Engineer Research and Development Center
[8]USACE ERDC

November 23, 2022

Abstract

The mechanisms and geographic locations of tidal dissipation in barotropic tidal models is examined using a global, unstructured, finite element model. From simulated velocities and depths, the total dissipation within the global model is estimated. This study examines the effect that altering bathymetry can have on global tides. The Ronne ice shelf and Hudson Bay are identified as a highly sensitive region to bathymetric specification. We examine where dissipation occur and find that high boundary layer dissipation regions are very limited in geographic extent while internal tide dissipation regions are more distributed. By varying coefficients used in the parameterizations of both boundary layer and internal tide dissipation, regions that are highly sensitive to perturbations are identified. Particularly sensitive regions are used in a simple optimization technique to improve both global and local tidal results. Bottom friction coefficients are high in energetic flow regions, across the arctic ocean, and across deep ocean island chains such as the Aleutian and Ryuku Islands. Global errors of the best solution in the M_2 are 3.10 \si{cm} overall, 1.94 \si{cm} in areas deeper than 1000 \si{m}, and 7.74 \si{cm} in areas shallower than 1000 \si{m}. In addition to improvements in tidal amplitude, the total dissipation is estimated and compared to astronomical estimates. Greater understanding of the geographical distribution of regions which are sensitive to friction allows for a more efficient approach to optimizing tidal models.

Dissipation and Bathymetric Sensitivities in an Unstructured Mesh Global Tidal Model

Coleman P. Blakely[1], Guoming Ling[1], William J. Pringle[2], María Teresa Contreras[1], Damrongsak Wirasaet[1], Joannes J. Westerink[1], Saeed Moghimi[3,4], Greg Seroka[3], Lei Shi[3], Edward Myers[3], Margaret Owensby[5], Chris Massey[5]

[1]Department of Civil and Environmental Engineering and Earth Sciences, University of Notre Dame, Notre Dame, IN, USA
[2]Environmental Science Division, Argonne National Laboratory, Lemont, IL, USA
[3]NOAA National Ocean Service, Office of Coast Survey, National Oceanic and Atmospheric Administration, Silver Spring, MD, USA
[4]University Corporation for Atmospheric Research, Boulder, CO, USA
[5]Coastal and Hydraulics Laboratory, Engineer Research and Development Center, U.S. Army Corps of Engineers, Vicksburg, MS, USA

Key Points:

- Bathymetric perturbations in key locations can change global tides more than any dissipation process.
- Boundary layer dissipation is concentrated in a small portion of the ocean while baroclinic conversion is more distributed.
- Frictional coefficients derived via optimization methods are consistent with regional physical and hydrodynamic characteristics.

Corresponding author: Coleman P. Blakely, `cblakely@nd.edu`

Abstract

The mechanisms and geographic locations of tidal dissipation in barotropic tidal models is examined using a global, unstructured, finite element model. From simulated velocities and depths, the total dissipation within the global model is estimated. This study examines the effect that altering bathymetry can have on global tides. The Ronne ice shelf and Hudson Bay are identified as a highly sensitive region to bathymetric specification. We examine where dissipation occur and find that high boundary layer dissipation regions are very limited in geographic extent while internal tide dissipation regions are more distributed. By varying coefficients used in the parameterizations of both boundary layer and internal tide dissipation, regions that are highly sensitive to perturbations are identified. Particularly sensitive regions are used in a simple optimization technique to improve both global and local tidal results. Bottom friction coefficients are high in energetic flow regions, across the arctic ocean, and across deep ocean island chains such as the Aleutian and Ryuku Islands. Global errors of the best solution in the M_2 are 3.10 cm overall, 1.94 cm in areas deeper than 1000 m, and 7.74 cm in areas shallower than 1000 m. In addition to improvements in tidal amplitude, the total dissipation is estimated and compared to astronomical estimates. Greater understanding of the geographical distribution of regions which are sensitive to friction allows for a more efficient approach to optimizing tidal models.

Plain Language Summary

This paper studies how and where tides dissipate energy. Using current speeds and water levels, it is possible to estimate how much energy the ocean dissipates and find areas that are particularly energetic. An important aspect of tidal modelling is accurately setting the depth of the ocean. We identify areas of the ocean where it is very important to have accurate water depths for accurate results by using different bathymetric datasets. Additionally, we find what areas of the ocean are sensitive to changes in energy dissipation. This is done via altering frictional coefficients in our model for both friction between the ocean floor and the bottom of the water column, and for internal waves that are generated near steep topography with strong vertical density gradients. With this information, a simple technique is used to determine optimal friction coefficients, improving the tides in our model by over half a centimeter globally, by almost a centimeter in the deep ocean, and by a little less than half a centimeter in shallow regions.

1 Introduction

The primary dissipation mechanisms for global tides are boundary layer dissipation and internal tide dissipation from baroclinic to barotropic tidal conversion (Munk, 1997). Estimates of the total tidal dissipation have ranged widely as knowledge of physical systems has grown. From early estimates of total tidal dissipation characterized solely by boundary layer dissipation by Taylor and Shaw (1920) and Jeffreys (1921) in the early 20th century using energy fluxes, to sophisticated estimates using altimeter data and assimilated tidal models performed by Egbert and Ray (2001) and Green and Nycander (2013), our understanding of where the astronomical energy imparted on the oceans is dissipated has grown tremendously. Several of these studies use the geographical distribution of energy dissipation as a method to better understand the physical realities that govern tidal dynamics.

The numerical model used in this study is based on recent developments of the Advanced Circulation Ocean Model (ADCIRC) and the mesh generation toolbox Ocean-Mesh2D. The former is a finite-element method shallow water equation solver used for modeling of regional, coastal, and global ocean systems (Westerink et al., 2008; Pringle et al., 2021). The latter allows for the creation of high quality, global to channel scale,

unstructured triangulated meshes driven by geometric and hydrodynamic characterization parameters (Roberts et al., 2019a). This tidal model can, in turn, be used to ascertain the geographical location of tidal dissipation Our mesh resolution varies between 2.5 and 25 km and strategically focuses resolution on areas with geometric complexity and large bathymetric gradients (Pringle et al., 2021).

Before examining frictional sensitivities, we believe that it is important to put in context the magnitude of sensitivities to frictional changes by exploring how changes in bathymetry within our model can effect tides. X. Wang et al. (2021) shows that certain regions are highly sensitive to bathymetric perturbations. This would suggest that improving bathymetry in specific locations models will have a significant impact on global tides. With the continued improvement and availability of global bathymetric datasets such as the GEBCO Bathymetric Group gridded bathymetry data and numerous high-fidelity local/regional bathymetric datasets it is vital to assess how these different data sources can impact tidal results. We will show that bathymetric improvements in select areas can have disproportionate impacts on global tidal results and are a vital control on improving modeled tides.

Following the study of bathymetry, we subsequently identify regions within our global model that dissipate a large amount of tidal energy. Based on this geographic distribution of dissipation density, we use a targeted approach to investigate what regions are particularly sensitive to perturbations in parameterizations of both boundary layer and internal tide dissipation.

With knowledge of where and how dissipation occurs in our model, a careful study of both internal tide and boundary layer dissipation is performed. Locations of high sensitivity are examined and reasons for their sensitivity are discussed.

There have been numerous studies on using frictional tuning parameters to improve tidal results. Approaches have varied from methodical searches of what parameters provide the best results (Lyard et al., 2006, 2021), using bedform information to select values for the open ocean (Pringle et al., 2018a), adjoint-type methodologies for selecting optimal coefficients (Graham et al., 2017; Qian et al., 2021; D. Wang et al., 2021) and, in the case of overland flooding, using land use information to select values (Bunya et al., 2010). Our investigation suggests that through careful consideration of which areas of the globe are most sensitive to frictional perturbations, and through the use of cost function minimization, it is possible to more efficiently find optimal friction coefficients for these sensitive areas, resulting in a high fidelity global tidal model. We also find that these optimal parameters are consistent with the physical and hydrodynamic characteristics of the targeted regions.

2 Model Setup and Methods

2.1 Governing Equations

The governing equations used in this study are the non-conservative shallow water equations (SWE). These are depth averaged Navier-Stokes equations commonly used in tidal modeling. The form of these equations used by ADCIRC are written in spherical coordinates as (Westerink et al., 1994; Pringle et al., 2021):

$$\frac{\partial \eta}{\partial t} + \frac{1}{R\cos\phi}\left[\frac{\partial(UH)}{\partial\lambda} + \frac{\partial(VH\cos\phi)}{\partial\phi}\right] = 0, \tag{1}$$

$$\frac{\partial U}{\partial t} + \frac{g}{R\cos\phi}\frac{\partial\eta}{\partial\lambda} = -\frac{U}{R\cos\phi}\frac{\partial U}{\partial\lambda} - \frac{V}{R}\frac{\partial U}{\partial\phi} + \frac{g}{R\cos\phi}\frac{\partial}{\partial\lambda}\big(\eta_{EQ} + \eta_{SAL}\big)$$
$$-\Big(C_{\lambda\phi} - f\Big)V - \Big(\frac{C_d\sqrt{U^2+V^2}}{\rho_0 H} + C_{\lambda\lambda}\Big)U \tag{2}$$
$$+\frac{1}{RH}\left[\frac{\partial\tau_{\phi\phi}}{\partial\phi} + \frac{1}{\cos\phi}\frac{\partial\tau_{\phi\lambda}}{\partial\lambda} + \tan\phi\big(\tau_{\lambda\lambda} - \tau_{\phi\phi}\big)\right]$$

$$
\begin{aligned}
\frac{\partial V}{\partial t} + \frac{g}{R}\frac{\partial \eta}{\partial \phi} = &-\frac{U}{R\cos\phi}\frac{\partial V}{\partial \lambda} - \frac{V}{R}\frac{\partial V}{\partial \phi} - \frac{g}{R}\frac{\partial}{\partial \phi}\big(\eta_{EQ} + \eta_{SAL}\big) \\
&- \Big(C_{\phi\lambda} + f\Big)U - \Big(\frac{C_d\sqrt{U^2+V^2}}{\rho_0 H} + C_{\phi\phi}\Big)V \\
&+ \frac{1}{RH}\bigg[\frac{1}{\cos\phi}\frac{\partial \tau_{\lambda\lambda}}{\partial \lambda} + \frac{\partial \tau_{\lambda\phi}}{\partial \phi} + \tan\phi\big(\tau_{\lambda\lambda} - \tau_{\phi\phi}\big)\bigg]\bigg]
\end{aligned}
\tag{3}
$$

where η is the water surface elevation; R is the radius of the earth; U and V are the depth averaged velocities in the zonal and meridional directions; $H = h + \eta$ is the total water column with h being the still water depth; $f = 2\Omega\sin\phi + \frac{\tan\phi}{R}U$ is the Coriolis parameter and advection in spherical coordinates with Ω being the angular velocity of the earth and ϕ being the latitude; η_{EQ} is the equilibrium tide; η_{SAL} is the self-attracting and loading term; and C_d is the dimensionless bottom drag coefficient. Additional terms are:

$$
\boldsymbol{C} = \begin{bmatrix} C_{\lambda\lambda} & C_{\lambda\phi} \\ C_{\phi\lambda} & C_{\phi\phi} \end{bmatrix} = \text{internal wave drag tensor}
$$

$$
\begin{aligned}
\boldsymbol{\tau} &= \begin{bmatrix} \tau_{\lambda\lambda} & \tau_{\lambda\phi} \\ \tau_{\phi\lambda} & \tau_{\phi\phi} \end{bmatrix} = \text{lateral stress tensor} \\
&= \begin{bmatrix} 2\upsilon_t H\frac{1}{R\cos\phi}\frac{\partial U}{\partial \lambda} & \upsilon_t H\big[\frac{1}{R}\frac{\partial U}{\partial \phi} + \frac{1}{R\cos\phi}\frac{\partial V}{\partial \lambda}\big] \\ \upsilon_t H\big[\frac{1}{R}\frac{\partial U}{\partial \phi} + \frac{1}{R\cos\phi}\frac{\partial V}{\partial \lambda}\big] & 2\upsilon_t\frac{H}{R}\frac{\partial V}{\partial \phi} \end{bmatrix}
\end{aligned}
$$

A further explanation of the internal wave drag tensor is provided in Section 2.2.1. The lateral stress parameterization used is a symmetrical Smagorinski closure model where υ_t is the Smagorinski lateral eddy viscosity coefficient (Smagorinsky, 1963; Dresback et al., 2006).

While the physics of tides are largely barotropic, there are several baroclinic effects that can have noticeable effects on solutions. Among these, the most important is the dissipation due to baroclinic conversion discussed in Section 2.2.1. For this study, internal wave stresses are estimated by using decadally-averaged salinity and temperature fields from the World Ocean Database (WOD) (Boyer et al., 2013). Using the temperature and salinity information, the wave drag tensor is calculated using a local generation formulation (Pringle et al., 2018a). Other baroclinic effects that are not captured involve baroclinicly driven ocean circulation, steric effects, and the seasonality of vertical density structures that determine baroclinic wave generation.

2.2 Calculation of Dissipation

Numerous forms of both internal tide and boundary layer dissipation have been used to parameterize energy loss due to internal wave generation and turbulence in the bottom boundary layer respectively. Two characterizations have been chosen for each form of dissipation and their performance will be examined in Section 5.

2.2.1 Internal Tide Dissipation

The internal wave drag tensor $\boldsymbol{C}$ in Equations 2 and 3 is either the scalar or directional drag coefficient of the linear frictional drag formula for internal tide dissipation due to baroclinic to barotropic conversion. Prior studies have suggested this dissipation mechanism has a large impact in global models, especially in areas with steep bathymetric gradients coincident with strong vertical density gradients (Egbert & Ray, 2000). For the purposes of this study, the "local" parameterization from Pringle et al. (2018a) was used. This parameterization assumes that internal waves are generated perpendicular to steep bathymetric gradients and are only affected by local topography and density gradients. In addition to the directional parameterization used in Pringle et al. (2018a),

149 a scalar parameterization that uses the magnitude of the topographic slope is examined.
150 The directional and scalar parameterizations are, respectively:

$$\boldsymbol{C}_{directional} = C_{it} \frac{\sqrt{(N_b^2 - \omega^2)(\bar{N}^2 - \omega^2)}}{\omega} \begin{bmatrix} h_\lambda^2 & h_\lambda h_\phi \\ h_\lambda h_\phi & h_\phi^2 \end{bmatrix}, \tag{4}$$

$$C_{scalar} = C_{it} \frac{\sqrt{(N_b^2 - \omega^2)(\bar{N}^2 - \omega^2)}}{\omega} \sqrt{h_\lambda^2 + h_\phi^2} \tag{5}$$

151 where, C_{it} is a dimensionless tuneable scale factor; N_b is the Brunt-Väisälä frequency
152 calculated at the seabed; ω is the dominant tidal frequency (M_2 in this study); $\bar{N}$ is the
153 depth-averaged Brunt-Väisälä frequency; and h_λ and h_ϕ are the bathymetric slopes in
154 the zonal and meridional directions. Both N_b and $\bar{N}$ are estimated from temperature
155 and salinity fields from WOD (Boyer et al., 2013). For this study, a cutoff depth above
156 which internal tide dissipation is ignored was set at 150 meters because boundary layer
157 dissipation becomes the dominant dissipation mechanism in shallow regions (Pringle et
158 al., 2018a).
159 An important note is that h_λ and h_ϕ are calculated directly from bathymetric datasets
160 and not from our model. Bathymetric gradients are assigned using a cell-averaged ap-
161 proach that calculates the root mean square of the differences in height contained within
162 the elements attached to a node (Roberts & Pringle, 2018). This approach accentuates
163 steep regions more than a simple cell averaging technique. For all cases in this study, bathy-
164 metric slopes were calculated from GEBCO2020 in order to eliminate discrepancies be-
165 tween models.
166 One important consideration when selecting C_{it} is the mesh dependency of the co-
167 efficient. Both mesh resolution and bathymetry can impact the optimum tuning coef-
168 ficient. While directly using the source bathymetric data and applying the cell-averaged
169 approach removes these impacts to a degree, it does not elimitate them entirely.

2.2.2 Boundary Layer Dissipation

171 Boundary layer dissipation is determined by the quadratic friction law $C_d|\boldsymbol{u}|\boldsymbol{u}$. The
172 bottom drag coefficient (C_d) can be calculated in several ways. Commonly, the coeffi-
173 cient is treated as a constant on the order of 3×10^{-3}. Previous studies have suggested
174 that changing these values between commonly used values of 1×10^{-3} up to 1×10^{-2}
175 have little global effect but can result in improved results regionally, especially on shelves
176 and floodplains (Pringle et al., 2018a; Lyard et al., 2006). In this study, we show that
177 while this is generally the case, altering the bottom friction in specific regions around
178 the globe can have significant, basin-scale impacts on tidal results.
179 An alternative strategy for calculating a bottom friction coefficient is through the
180 use of Manning's n coefficients and a depth-dependent relationship with C_d. Originally
181 developed for use in open channel flow, Manning's equation has been widely used to pa-
182 rameterize frictional losses in rivers, over floodplains, and in coastal and ocean flows (Arcement
183 & Schneider, 1989). Manning's n values are selected through characterization of sedi-
184 ment in a region, how much vegetation is present, any bends in rivers, and other bed-
185 form factors that could affect friction (Chow, 1959; Arcement & Schneider, 1989). These
186 Manning's n values are converted to bottom drag coefficients in the governing equations
187 using the following relationship (Atkinson et al., 2011):

$$C_d = \frac{gn^2}{H^{1/3}} \tag{6}$$

188 where n is the selected Manning's n coefficient generally in the range of 0.012 to 0.05 $\mathrm{s\,m^{-1/3}}$
189 in the ocean and can be much higher overland. A commonly used Manning value for the
190 open ocean is 0.022 $\mathrm{s\,m^{-1/3}}$ (Atkinson et al., 2011; Kerr et al., 2013). The inclusion of
191 the extra $H^{-1/3}$ depth dependency in the calculation of the bottom drag coefficient re-
192 sults in higher boundary layer dissipation in shallow regions and lowers it in the deep
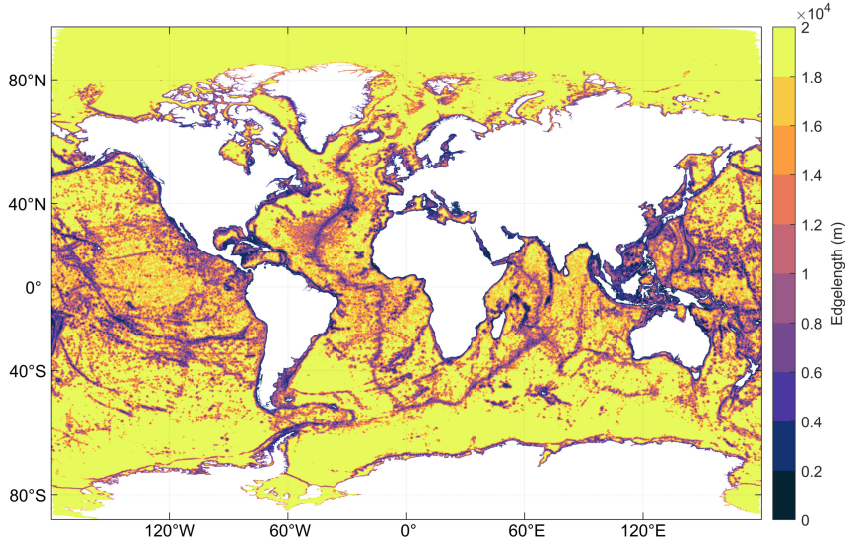
Figure 1. Resolution of the global mesh used in this study. The effect of the topographic length scale can clearly be seen along ocean ridges, mountain chains, and shelf breaks. Minimum resolution is 2 kilometers, maximum is 25 kilometers.

shelf and ocean regions, redistributing the boundary layer dissipation to regions where it is known to occur (Munk & Wunsch, 1998).

2.3 Finite Element Grid

For this study, a global, unstructured mesh was generated using OceanMesh2D 3.3 (Roberts et al., 2019a). The resolution ranges from 25 km in the deep ocean down to 2 km in coastal areas. The final mesh contained approximately 3.7 million nodes and 7.1 million elements. The resolution of the finished mesh can be seen in Figure 1. While numerous parameters determine edgelength in OceanMesh2D, of particular importance for this study is the topographic length scale, which ensures that steep topography is well resolved (see Roberts et al. (2019a); Pringle et al. (2021) for a description of other parameters used, including medial axes, expansion rates, wavelength to mesh size ratio, etc.) (Roberts et al., 2019b). Resolution targeted in regions with steep bathymetry efficiently places higher resolution in key regions of the ocean. As Figure 1 shows, this mesh has targeted resolution over mid ocean ridges, at shelf breaks, and over submerged mountain chains. By placing high resolution in such areas, the baroclinic conversion can be more accurately resolved, allowing for this mesh to better capture deep ocean dissipation. Boundary layer dissipation is already well resolved because it is focused mainly in shallow and coastal regions which already have high resolution. Bathymetric datasets used to develop this mesh are described and analyzed in Section 4. Due to the shallow nature and complex shorelines in areas with high boundary layer dissipation, these regions—Hudson Bay, Bay of Fundy, etc.—are also highly resolved due the depth-dependent and feature size edgelength functions. For all simulations, a minimum depth of 5 m was enforced.

2.4 ADCIRC Implementation

Simulation in this study were executed using version 55 of the ADCIRC model, a finite element based 2D/3D shallow water equation solver which considers the reformulation of the continuity equation into the generalized wave continuity equation (Luettich

& Westerink, 2004; Pringle et al., 2021). This reformulation is performed by differentiating the continuity equation with respect to time, weighting the primitive continuity equation with a weighting parameter τ_0, and adding the two equations together. AD-CIRC is notable for its low numerical dissipation and its high degree of scalability (Tanaka et al., 2010). Several modifications were made in version 55 that enable the modeling of global domains (Pringle et al., 2021). These modifications include rotating the poles to pass through land locations to remove the spherical coordinate systems singularity and allow for better formed elements near the poles; corrections to the governing equations in a global cylindrical projection system; and reformulation of variables to eliminate overly systems of equations at high latitudes. Additionally, careful weighting of the temporal scheme to allow for significantly larger time steps and improved computational efficiency. In addition to the methods of dissipation discussed above, there is also minimal loss due to numerical diffusion. By carefully selecting the weighting parameter τ_0, it is possible to improve numerical dispersion properties and better capture phases of tidal propagation (Atkinson et al., 2004a, 2004b). For this model, a value of $\tau_0 = 8/(5\Delta t) = 0.027$ was used to satisfy stability constraints (Pringle et al., 2021).

Simulations were forced with the M_2, Q_1, O_1, P_1, K_1, N_2, S_2, and K_2 astronomical tides. Due to the changes to v55 of ADCIRC, it was possible to use a time step of 60 seconds without degrading temporal accuracy. Tidal analysis was performed over a 180 day period with a 30 day spin up period to dampen any transients from the cold start of the model. For the perturbation runs described in Section 5, a shorter run was possible because the M_2 tide was the only constituent considered. As such, perturbation simulations were run for 45 days with a 15 day spin up. The Smagorinsky coefficient (υ_t) which controls lateral eddy viscosity was set to a value of 0.05 for all simulations. Results showed little to no sensitivity to the selection of υ_t.

2.5 Methods of Analysis

In order to analyze the accuracy of this model, tidal harmonics were used and a number of error metrics were calculated. To evaluate both the amplitude and phase of the error in one metric, the root mean square discrepancy (D) was used (X. Wang et al., 2012):

$$D = \sqrt{0.5 \sum_k \left[\left(A_o^k\right)^2 + \left(A_m^k\right)^2 - 2A_o^k A_m^k \cos\left(\theta_o^k - \theta_m^k\right) \right]} \tag{7}$$

where A and θ are amplitude and phase, k denotes the kth constituent, o denotes observed, and m denotes modelled. This metric was calculated at the centroid of each element by interpolating TPXO9-atlas (hereafter TPXO9) and model result (Egbert & Erofeeva, 2002, 2021). TPXO9 was selected as a reference solution due to its high accuracy compared to tide gauges in open water regions. In deep water, TPXO9 has a mean error compared to gauges of 0.5 cm; in shallow regions of 3.19 cm; and in coastal regions of 3.03 cm (Stammer et al., 2014). All regions shallower than 20 meters were omitted from the calculation of error metrics due to lower accuracy of TPXO9 in coastal and inlet systems, inadequate resolution of complex inlet systems within our mesh, and lack of high resolution bathymetric data. To turn D into a single global metric, the area weighted mean of the discrepancy compared to TPXO9 ($\bar{D}_{tpxo}$) was used:

$$\bar{D}_{tpxo} = \frac{\sum_i A_i D_i}{\sum_i A_i} \tag{8}$$

where A_i is the area of the ith element and D_i is the discrepancy at the centroid of the ith element.

In addition to computing the mean discrepancy to TPXO9, results were also compared to a compilation of global tide datasets (Pringle, 2017). Stations used for analysis were limited to ensure that they fell within the model domain and that sufficient resolution existed at their locations for an accurate analysis. A list of the specific stations used, as well as the amplitudes and phases from Pringle (2017) is available from

Blakely (2021). For these stations, the discrepancy, mean amplitude error, absolute mean amplitude error, standard deviation, R^2, and average error were computed.

3 Dissipation Estimation

As an additional measure of model skill, the total tidal energy dissipated was estimated and compared to estimates of global tidal dissipation. This calculation was performed using velocity and elevation outputs from simulations. Velocity and elevation were output at 30 minute intervals over 180 days of simulation to find time averaged dissipation rates. Terms for boundary layer and internal tide stress are:

$$\boldsymbol{\tau_{bl}} = \rho_0 C_d \left| \boldsymbol{u} \right| \boldsymbol{u} \tag{9}$$

$$\boldsymbol{\tau_{it}} = H\rho_0 \boldsymbol{C} \cdot \boldsymbol{u} \tag{10}$$

where ρ_0 is the reference density of water, C_d is the bottom friction coefficient defined as either constant or derived from Manning's n, $\boldsymbol{u}$ is the depth averaged velocity vector, and $\boldsymbol{C}$ is either the directional internal wave tensor, or the scalar internal wave coefficient.

Using the above drag forces, the dissipation due to boundary layer friction and internal wave turbulence are found to be:

$$D_{bl} = \boldsymbol{u} \cdot \boldsymbol{\tau_{bl}} = \rho_0 C_d \left| \boldsymbol{u} \right|^3 \tag{11}$$

$$D_{it} = \boldsymbol{u} \cdot \boldsymbol{\tau_{it}} = \rho_0 \boldsymbol{u} \cdot \boldsymbol{C} \cdot \boldsymbol{u} \tag{12}$$

where all variables have the same meanings as defined in equations 1, 2, 3 9, and 10. In order to find total dissipation, these dissipation rates were time averaged and then integrated over the whole domain of the simulation. Thus, the total dissipation for boundary layer friction and internal tide generation are found to be

$$D_{bl,total} = \int_A \left[\frac{1}{T} \int_{t=t_0}^{t=t_f} D_{bl} dt \right] dA \tag{13}$$

$$D_{it,total} = \int_A \left[\frac{1}{T} \int_{t=t_0}^{t=t_f} D_{it} dt \right] dA \tag{14}$$

respectively. This method is different than that implemented in Egbert and Ray (2000, 2001), wherein the dissipation was calculated from a formula based on the balance between the so-called work rate and tidal energy flux using tidal amplitudes and volume fluxes. The advantage of using the parameterizations of stress to estimate dissipation are that it is possible to split the dissipation mechanisms clearly between internal tide conversion and boundary layer dissipation. Using the local balance formula, it is necessary to make assumptions about the locations of boundary layer and internal tide dissipation, i.e., it is necessary to assume that shallow regions are dominated by boundary layer dissipation and deep areas are dominated by internal tide dissipation (Munk & Wunsch, 1998; Egbert & Ray, 2000, 2001; Green & Nycander, 2013). Additionally, by using the direct formula, dissipation rates are always positive, whereas using the balance formula, this is not always the case.

4 Bathymetric Sensitivities

Later in this paper, we demonstrate that it is possible to improve results for a tidal model by carefully selecting parameters that govern energy dissipation; however, the best way to improve results in simulations is to use the most accurate bathymetry available. High quality bathymetry is particularly important in key areas of high sensitivity.

In order to understand the impact of bathymetry on model results, a selection of data sets were assigned to mesh nodes based on a cell-averaged approach and 45-day tidal simulations were performed (Roberts & Pringle, 2018). Hereafter, when it is mentioned

Table 1. Summary of bathymetric datasets.

Data Set	Source	Resolution	Coverage
GEBCO 2014 Grid	GEBCO (2014)	30 arc-second	Global
GEBCO 2019 Grid	GEBCO (2019)	15 arc-second	Global
GEBCO 2020 Grid	GEBCO (2020)	15 arc-second	Global
CHS NONNA 100	CHS (2018)	100 meter	Canadian Territorial Waters
RTopo-2	Schaffer et al. (2019)	30 arc-second	Greenland and Antartica
nthaus100	Beaman (2018)	100 meter	Northwest Australia/Timor Sea

that bathymetry was interpolated onto the mesh, this cell-averaged interpolation is the method used. All experiments used a directional C_{it} of 2.5 and a Manning's n of 0.022 $s\,m^{-1/3}$ in the majority of the ocean and 0.028 $s\,m^{-1/3}$ in the high dissipation regions defined in Section 5. We consider combinations of bathymetry from six different datasets, namely, GEBCO2014, RTopo-2, GEBCO2019, CHS NONNA-100, nthaus100, and GEBCO2020 (see Table 1 for a summary of these datasets). Figure 2 shows the response in the M_2 amplitude due to using various combinations of the bathymetric datasets.

A shortcoming, for tidal modeling, of the GEBCO datasets is their representation of the Arctic and Greenland ice shelves. Within GEBCO versions 2014, 2019, and 2020, altimeter data is used over these ice shelves. In Figure 3, this results in ice sheets being represented in GEBCO by the ice shelf surface elevation (H_{se}) depicted in Figure 3. In contrast, RTopo is composed of three different datasets: "bedrock topography," or bathymetric depth without the presence of ice (H); "ice base topography," or the location in reference to the geoid of the ice draft (H_{ib}); and the "surface elevation," or the height above the geoid of the surface (H_{se}).

When only a GEBCO dataset is used, any part of the mesh that was underneath the ice shelf was represented as land and therefore set to a minimum depth of 5 meters. Clearly, this treatment will not result in accurate volume fluxes underneath ice shelves. Instead a physically consistent value to use under ice shelves is the difference between the bedrock topography and ice base topography (in Figure 3, this value corresponds to $H - H_{ib}$) as prescribed in Pringle et al. (2021). Hereafter, it is noted that this treatment is used for all simulations with the RTopo dataset.

Figure 2a shows the difference in the M_2 amplitude between the simulation with only GEBCO2014 and the simulation with GEBCO2014 and RTopo. While it would be expected that drastically changing the bathymetry under the Arctic ice shelves would have a large effect on local tidal results, it is notable that this bathymetric change dramatically changed the tides all over the globe and particularly through the Atlantic basin. In this extreme case, changes in the M_2 amplitude of up to 20 cm were seen as far north as Baffin Bay. In order to investigate this phenomenon more closely, an additional simulation wherein the Ronne ice shelf bathymetry was interpolated from GEBCO2014 was performed. As discussed above, this had the effect of enforcing the minimum depth of 5 meters anywhere that the Ronne ice shelf covers. Everywhere else in and around Antartica, RTopo was used. Figure 2b shows the difference between this run and the run with only GEBCO2014. Using RTopo in Antartica everywhere but under the Ronne ice shelf did have global effects on the M_2 tide in the model; however, the response to this perturbation was nowhere near the magnitude of the response when RTopo is used under the Ronne ice shelf.

Strikingly, the Ronne ice shelf has a disproportionately large influence on the tides all the way through Baffin Bay and the North Sea. We hypothesize that this sensitivity is related to semi-diurnal, basin scale resonance throughout the Atlantic Basin, starting in Baffin Bay and extending all the way down to Antartica. By interpolating RTopo in addition to GEBCO2014, the bathymetry in the Weddell Sea, and specifically under the Ronne ice shelf, is deepened. This increases wave propagation speed nearshore in the
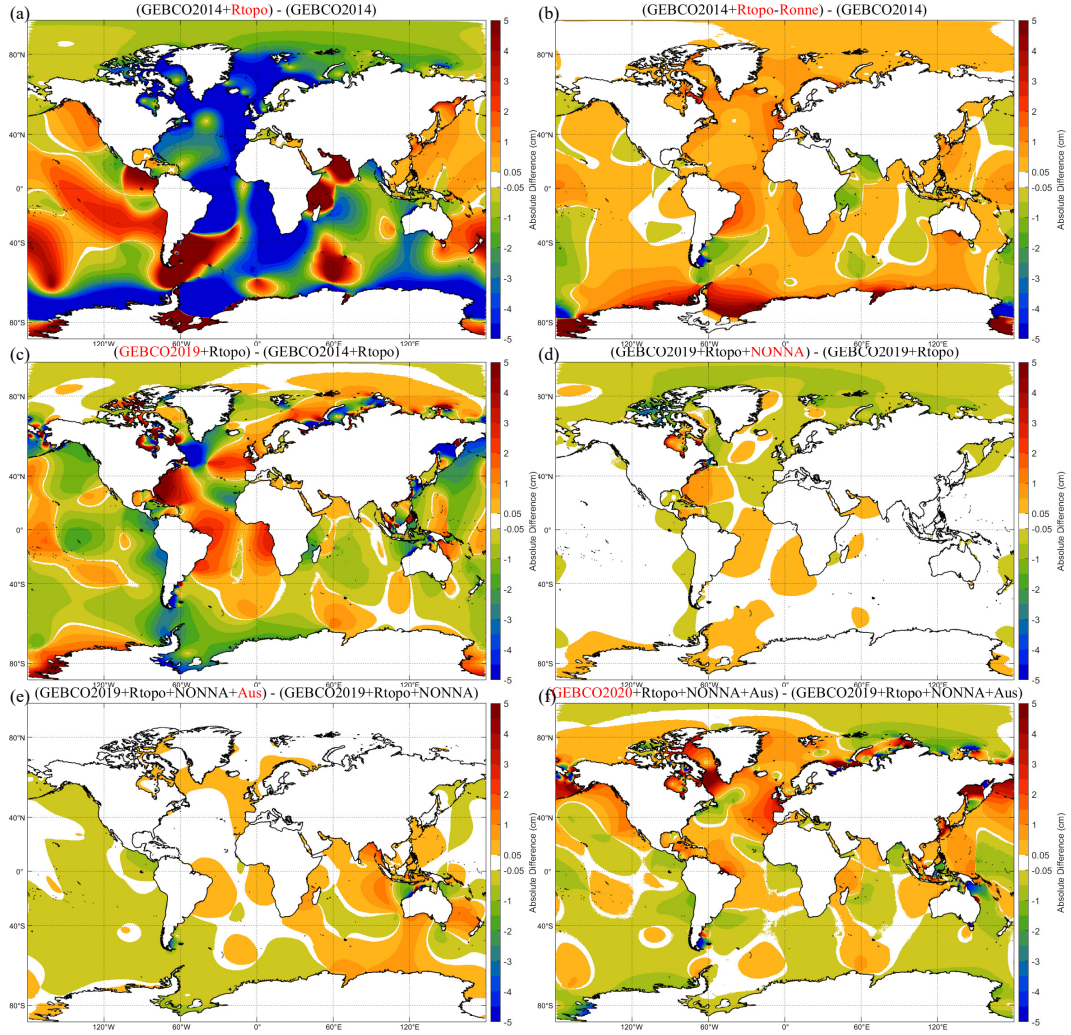
Figure 2. Changes in M_2 amplitude due to changes in bathymetry. (a) The primary difference in bathymetry here is the use of the height of the ice cavity as a bathymetric depth underneath the Antartic ice shelves. (b) In this sensitivity plot, the Ronne ice shelf is left as it is treated in GEBCO2014. The rest of Antartica uses RTopo. (c) Sensitivity from using GEBCO2019 in place of GEBCO2014; the resolution of GEBCO2019 is twice that of GEBCO2014 (d) Adding the CHS-NONNA100 dataset (which is already assimilated into GEBCO2019) does have an effect on the tides. (e) The inclusion of the nthaus100 grid (which primarily covers the Timor Sea) has similar magnitude effects to CHS-NONNA100. (f) Similar to upgrading from GEBCO2014 to GEBCO2019, the usage of GEBCO2020 has large magnitude effects on the tidal solution on a global scale.
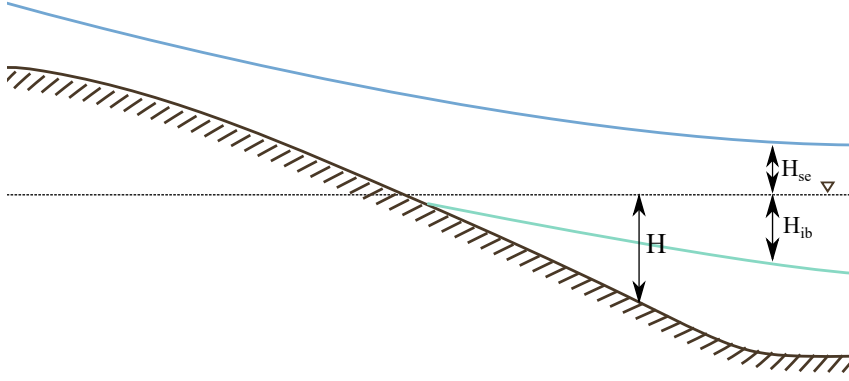
Figure 3. A visualization of the three RTopo quantities and what they contain. The black hatched line is the surface of the earth, the black dashed line is the reference datum (or GEOID), the blue line is the top of the ice sheet, and the green line the bottom of the ice sheet. H_{se} is the surface elevation. When no ice is present, this is just the surface topography. When ice is present it is the height above the GEOID of the top of the ice sheet. Over the ocean, where no ice is present, $H_{se} = 0$. H is the bedrock topography. This is simply the bathymetric depth or topographic height in the absence of an ice sheet. H_{ib} is the ice base topography. When the ice is land bound, this coincides with the bedrock topography. When the ice is floating, it is the ice draft.

Weddell Sea, changing the wavelength of a resonant wave in the Atlantic. Additionally, by shortening or lengthening ice shelves, the length of the Atlantic Basin is altered, allowing the wave to near resonance. Arbic et al. (2009) found that by blocking the Hudson Strait in tidal simulations, the effect on the Atlantic basin was to drastically increase the M_2 amplitude throughout the North Atlantic. They found that in resonant systems, there is a "back effect" on the open ocean when key areas of tidal resonance are altered. In the case of our treatment of the Ronne ice shelf, we perform the inverse of Arbic et al. (2009) and "un-block" the Weddell Sea. The effect in our case is also inverted, with the M_2 tide decreasing drastically. The nature of this sensitivity is highly interesting and certainly warrants more in depth study. In X. Wang et al. (2021), an in depth bathymetric sensitivity analysis was performed, wherein regions' bathymetry was perturbed randomly and areas with high sensitivity were identified. That study also finds that global tides are extraordinarily sensitive to perturbations in bathymetry of the Ronne ice shelf and the Weddell Sea.

Figure 2c shows the difference in the M_2 amplitude of GEBCO2019+Rtopo compared to GEBCO2014+Rtopo. The biggest difference between the GEBCO2014 and GEBCO2019 datasets is that GEBCO2019 has twice the resolution of GEBCO2014 (15 arc-seconds vs 30 arc-seconds). An additional difference between the datasets is the number of datasets assimilated into the global grid. GEBCO2014 has limited datasets and thus has to rely heavily on ship soundings. GEBCO2019 assimilates many more high-resolution datasets including CHS-NONNA100 and the nthaus100 dataset. The usage of localized datasets results in a significantly higher quality product and more accurate representations of bathymetry within the ADCIRC model used in this study.

While the use of GEBCO2019 does not result in nearly the magnitude of response as that from the inclusion of RTopo, it does significantly impact tides all over the globe. Throughout the Pacific, the response to using GEBCO2019 is ±3 centimeters while in the Atlantic it reaches as high as +20 centimeters along the US east coast. Once again, the Atlantic appears more sensitive to these bathymetric changes than the Pacific. The explanation is the improved representation of bathymetric depth in GEBCO2019 in the

Hudson and Baffin Bays. The Hudson Bay is one of the largest tidal dissipators in the world, dissipating between 200 and 350 GW of the total estimated 1.5 to 2 TW globally (Egbert & Ray, 2001). One of the datasets incorporated into GEBCO2019 that is absent in GEBCO2014 is CHS-NONNA100, a 100 meter resolution dataset covering Canadian waters including the Hudson and Baffin Bays. Inclusion of this dataset, even resampled to the 15 arc-second resolution of GEBCO2019, results in large differences in tides in the North Atlantic as can be seen in Figure 2c.

Due to the importance of correctly resolving the Hudson and Baffin Bays, the CHS-NONNA dataset in its original 100 meter resolution was independently interpolated onto the portion of the mesh within the CHS-NONNA coverage. The combination GEBCO2019+Rtopo+NONNA was compared to the combination GEBCO2019+Rtopo and the resulting response in the M_2 amplitude is depicted in Figure 2d. While GEBCO2019 does incorporate CHS-NONNA, Figure 2d clearly shows that the higher resolution of using the original dataset does have a noticeable effect. In the Arctic Ocean, the tidal response was a change in amplitude up to 2 centimeters in places. Additionally, the US East Coast is again impacted quite heavily, with a change of up to 3 centimeters in the Northeast. At first glance, this could be somewhat surprising since the mesh element size in the majority of the Hudson/Baffin bay areas is greater even than the 450 meter resolution of GEBCO2019. We attribute this to the cell-averaged method of bathymetric interpolation used in this study. This method of interpolation allows for much more physically consistent approximations of bathymetry which produces noticeable responses in the tides, especially in the North Atlantic and North Sea.

Another region with high dissipation is the Timor Sea/Northwest Australia. In order to examine the effect that higher resolution bathymetry had in that region, the nthaus100-grid dataset was interpolated onto our mesh (Beaman, 2018). Like CHS-NONNA, this dataset is a 100 meter resolution bathymetric dataset that was assimilated into GEBCO2019. Figure 2e shows the response on the M_2 tide due to the inclusion of this higher resolution bathymetry. Similar to the Hudson Bay and Baffin Bay, altering the bathymetry of the Timor Sea has modest non-local effects on tidal results in this model. Also like the Hudson and Baffin Bays, the Timor Sea has high velocity flows and large estimates of tidal boundary layer dissipation. This trend highlights the magnitude of improvement that higher quality bathymetry can have on tidal results, while also indicating that some areas are far more critical than others for bathymetric accuracy.

For completeness, GEBCO2020 was also used to compare the impact on tides that an updated global dataset would have. Like GEBCO2019, GEBCO2020 has 15 arc-second resolution. The differences between GEBCO2019 and GEBCO2020 are primarily the quality and number of assimilated datasets. Despite the resolution being identical, as Figure 2f shows that the updates to the GEBCO dataset resulted in substantial changes on global tidal results. Most heavily impacted are the Bering Sea, Hudson Bay, and the Ohkotsk Sea, all of which have responses over 5 centimeters in the M_2 tide.

Our bathymetric sensitivity investigation points to the significant impact that bathymetry has on tidal results. Highly accurate tidal results require high quality bathymetric data in specific areas. Certain regions, such as the Ronne Ice Shelf, the Weddell Sea, and Hudson Bay have impacts on global tidal results that other regions do not. Later in this paper, it will be shown that while altering frictional coefficients can impact tidal results, the magnitude of response to altering friction (up to around 1 or 2 cm) pales in comparison the effect of altering bathymetry in highly sensitive regions. The combination GEBCO2020+RTopo+NONNA+Aus provided the best solution of the various combinations of datasets and was used as the baseline for the rest of this study.

5 Sensitivity to Friction

5.1 Geographical Distribution of Dissipation

Estimates of tidal dissipation have historically split dissipation between shallow boundary layer dissipation and deep internal tide dissipation. It has long been accepted that most dissipation occurs due to boundary layer dissipation on the shelves and shallow regions of the ocean (Taylor & Shaw, 1920; Jeffreys, 1921). More recently, it has also been realized that a large amount of dissipation occurs in the deep ocean and across shelf breaks due to internal wave generation (Munk, 1997). Munk estimates that of the 3.7 TW of input energy from the sun and moon, 0.2 TW is lost to earth tides and 0.02 TW is lost to atmospheric tides. That leaves approximately 3.5 TW of energy to be dissipated due to dissipation in the ocean. How this energy is distributed between boundary layer and internal tide dissipation is somewhat uncertain. However, using altimetry data, Munk arrives at an estimate of 2.6 TW dissipated in the boundary layer and 0.9 TW in the internal tides, resulting in a 74%/26% split between boundary later and internal tide dissipation. In a more recent study Green and Nycander (2013) perform similar calculations using various parameterizations and find that in water deeper than 500 m, there is between 0.91 and 1.18 TW of dissipation, placing the proportion of internal tide dissipation between 26% and 34% of total tidal dissipation.

Beyond the split between shallow and deep water dissipation, there has been interest in finding exactly where geographically dissipation occurs within the ocean. Taylor and Shaw (1920) applied two different techniques—one using estimated energy fluxes and another using work performed by astronomical forcing—to the Irish Sea in order to estimate the boundary layer dissipation within that body of water. Expanding on that work, Jeffreys (1921) used similar techniques and applied them to other regions to find a very rough estimate of total tidal dissipation. Since then, numerous studies have been performed to more accurately find the locations, modes, and magnitudes of tidal dissipation. With the advent of projects such as the TOPEX/POSEIDON mission and subsequently highly accurate global tidal models such as TPXO, both altimetry (Egbert & Ray, 2001) and numerical models (Green & Nycander, 2013) have been used to estimate the location and magnitudes of not only the total tidal dissipation, but also the dissipation of specific tidal constituents.

For this study, it was hypothesized that, especially for boundary layer dissipation, only areas with high dissipation rates would be highly sensitive to frictional parameter adjustments. For that reason, and to perform a more targeted analysis of global sensitivities to changes in frictional parameters, an analysis of dissipation within the model was performed by examining the dissipation within each element as well as the total tidal dissipation from the formula described in Section 3. Figures 4a and 4b show, on a log scale, the boundary layer and internal tide dissipation, respectively, of our "best solution" model. Additionally, for reference, the maximum current speed and maximum tidal elevation are plotted in Figures 4c and 4d.

As expected, Figure 4a shows the vast majority of the boundary layer dissipation within the model occurs in shallow regions near the coast. Also as would be expected, the areas of highest dissipation have a combination of shallow bathymetry, high velocities (Figure 4c) and large tidal amplitudes (Figure 4d). In Figure 5, plots in the left column (Figures 5a, 5c, and 5e) display the areas that account for 50%, 90%, and 99% of boundary layer dissipation. In fact, based on this simulation, it was estimated that 90% of the boundary layer dissipation occurs in 1.4% of the surface area of the global ocean. This indicates that boundary layer dissipation is highly localized within just a few major dissipators.

Internal tide dissipation is far less localized as can be seen in Figure 4d. Within this model, it was determined that 90% of the internal tide dissipation occurred in 17.2% of the world oceans. Figure 5b, 5d, and 5f show the areas that account for 50%, 90%, and 99% of the internal tide dissipation in the model respectively. Clearly, this analysis indicates that baroclinic internal tide conversion and subsequent dissipation occurs
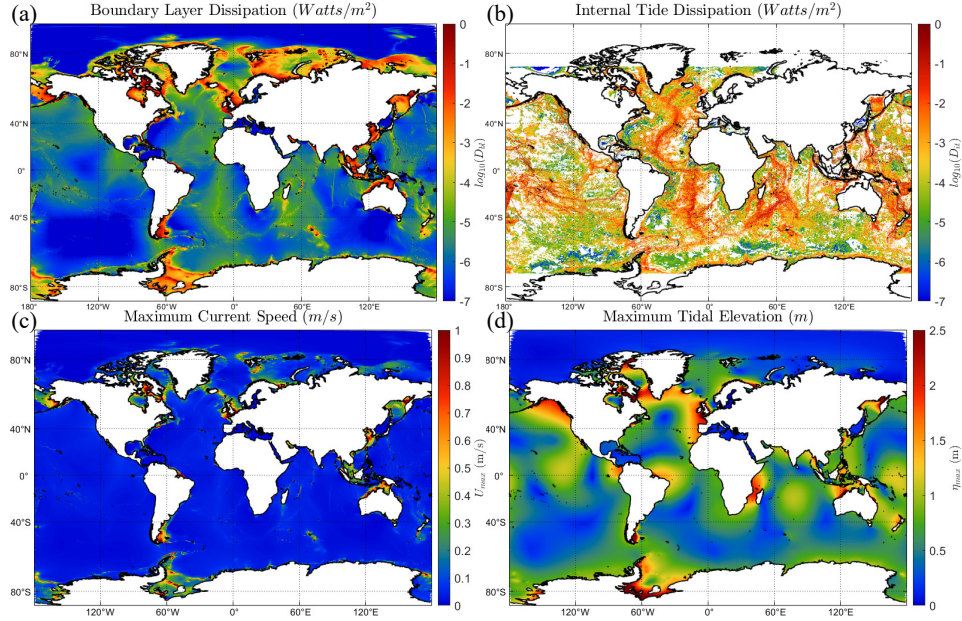
Figure 4. (a) Maximum current speed (m/s). (b) Boundary layer dissipation (W/m^2). (c) Maximum tidal elevations (m). (d) Internal tide dissipation (W/m^2). Note the use of logarithmic scales on the dissipation plots (b) and (d). Current speed and tidal elevation were taken from 30 day tidal simulations forced by the 8 dominant tidal constituents.

primarily along ridges, mountain ranges, and island chains in the deep ocean. The decision to place higher resolution in such regions certainly helps to resolve this dissipation and, ideally, produce higher quality tidal results.

5.2 Global Sensitivity to Friction Parameters

Prior to examining the responses of tides to changes in localized frictional parameters, we first studied tidal sensitivities to uniform change in friction parameters. In addition to better understanding the sensitivity to changes in globally constant friction parameters, this experiment also allowed for a comparison of the different parameterizations of internal tide dissipation (directional versus scalar C_{it}) and boundary layer dissipation (constant C_d or Manning's n). One important note is that due to the finding that boundary layer dissipation is highly localized, the majority of the model (mostly deep ocean and low velocity shelf regions) were left as commonly used values for both C_d or Manning's n. It is noted that perturbing botton friction values globally from standard values in most regions degrades local solutions. This was found to be especially true in low energy shelves and the deep ocean. In contrast, altering these friction values in high energy dissipation zones had effects locally as well as on a regional and basin scale.

Unlike boundary layer dissipation, the internal tide parameter C_{it} was altered globally. As Figure 4b shows, it is much harder to pinpoint areas of extremely high dissipation for internal tides. Additionally, the parameterization of internal tide dissipation automatically excludes many areas of low dissipation due to the parameterization being undefined at high latitudes and our depth cutoff of 150 m (any white space in Figure 4b).
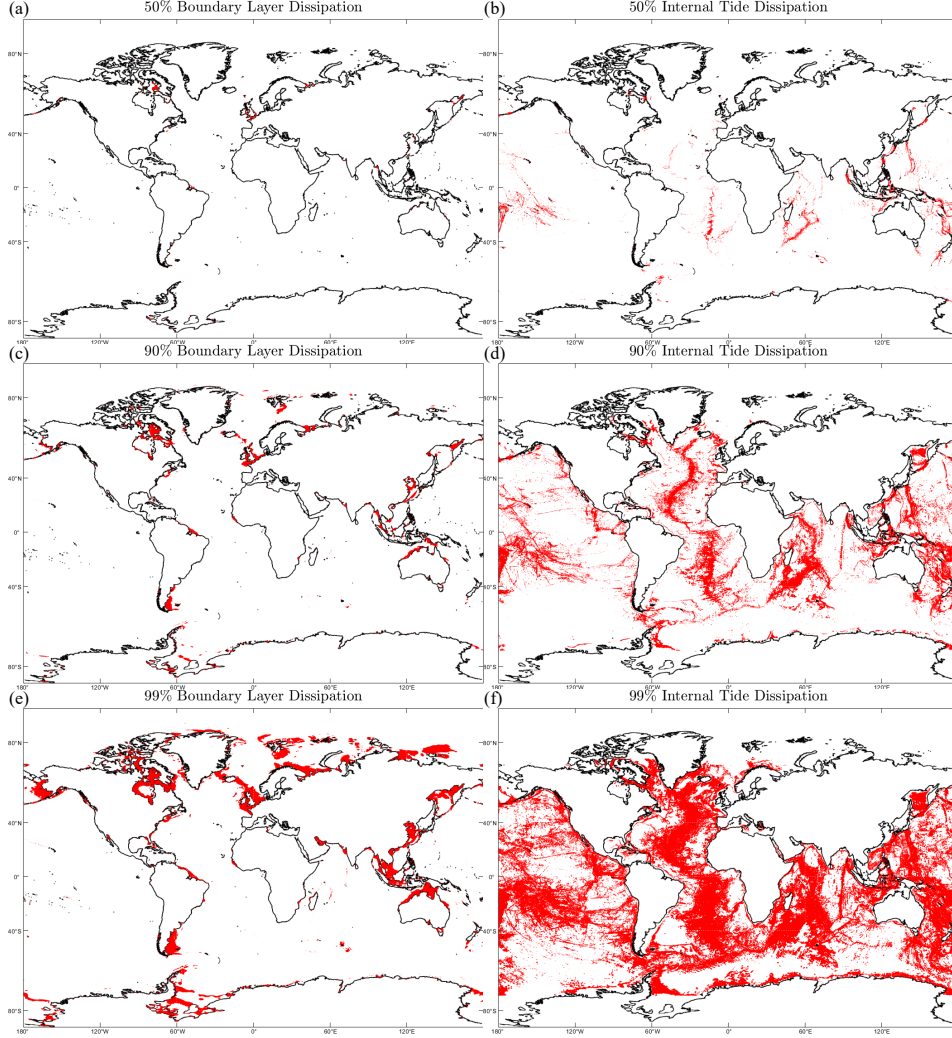
Figure 5.   (a), (c), and (e) show the areas that account for 50%, 90%, and 99% of dissipation within the ADCIRC model. The corresponding area ratios are 0.2%, 1.4%, and 4.3% of the model area respectively. (b), (d), and (f) show the same thing for internal tide dissipation with the area ratios being 2.3%, 16.7%, and 45.6% of the model area. Dissipation rates were interpolated to the centroids of each element. Elements were then sorted by dissipation rate in descending order and total dissipation per element was estimated via integration. In this manner, it was possible to find the least area that could account for 50%, 90%, and 99% of the total model dissipation.

5.2.1 C_d and Manning's n

Historically both C_d (Lyard et al., 2006; Egbert & Ray, 2001) and Manning's n (Bunya et al., 2010; Dietrich et al., 2011) have been used in the quadratic friction laws for modeling boundary layer dissipation in ocean models. ADCIRC supports both parameterizations and both have been tested extensively for both tide-only and extratropical and tropical storm surge cases. For the purposes of this study, we examined the efficacy of both in our global parameter study and select the more optimal parameterization.

Figure 6 shows the mean discrepancy compared to TPXO9 in various basins and marginal seas as a function of changed C_d or Manning's n. Of particular note is how gentle the slopes of the mean discrepancy are. As was expected, changing bottom friction does not have large effects on global solutions. However, certain regions seem to be quite sensitive to changed bottom friction. The marginal seas (Bering Sea, Japan Sea, Java Sea, and Yellow Sea) are noticeably more sensitive to bottom friction. Reasons for this disproportionate effect of bottom friction is due to the large island chains and shallow depths that characterize these areas. The Ryukyu and Aleutian Islands are extremely steep and contain shallow ridges and high current speeds. It is likely that the model is missing some unresolved lateral and vertical eddying associated with flows passing across very steep topography and through narrowly constrained island chains such as the Aleutian and Ryuku Islands. Further, our minimum 2.5 km resolution limits the ability of our model to capture this eddying in narrow, high energy regions.

For the Manning scheme, the majority of regions have relatively consistent minima at Manning values ranging from 0.026 to 0.030, while the Yellow Sea requires lower friction than the rest of the globe. This aligns with the findings in Pringle et al. (2018a), wherein seabed properties were used to estimate C_d for the Western Pacific and Indian Oceans. In that study, the values predicted for the Yellow Sea were significantly lower than the rest of the domain studied. As explained in Pringle et al. (2018a) in the study, the sediments in the Yellow Sea are quite silty and fine. As a consequence, lower values for both C_d and Manning's n are more optimal, explaining physically why this particular area has a minimum at a lower bottom friction coefficient than other regions which are not as homogeneously silty and clay-ey. Similarly in the C_d scheme, lower C_d yields better results in the Yellow Sea. Unlike the Manning scheme, there is not quite as much consistency in where the minima occur for the different regions. Instead, for example, the NE Pacific gets the best results at $C_d \approx 3.3 \times 10^{-3}$ while for the North Atlantic, $C_d \approx 1.9 \times 10^{-3}$ yields the best results.

Another important comparison is the impact of friction in coastal/shallow (20 to 1000 meters deep) compared to in the deep ocean. As past studies would suggest, for the majority of the ocean, the deep ocean is far less affected by changing the bottom friction than shallow regions. This is physically consistent with the parameterization of bottom friction, as the dependence on depth results in much lower boundary layer dissipation in deep regions than shallow ones. Furthermore, current speeds are simply lower in deeper waters.

From the numerical evidences described above, we prefer the Manning parameterization largely due to the minimum error for most basins and marginal seas (the Yellow Sea being the exception) having the lowest error at approximately $n = 0.028$. This is in contrast to the C_d parameterization where the improvement is much less consistent, with higher friction improving results in several basins while simultaneously degrading results in others. The Atlantic and southwest Pacific especially seem to be harmed by the use of higher C_d while in the Manning configuration, all basins except the Yellow Sea show consistent improvement with higher Manning's n. Additionally, Manning's n has many desireable characteristics suitable for the ultimate goal of this global model, which is to model integrated ocean to channel scale total water level driven by hurricanes, tropical storms, and other extreme weather events. It has been found that the extra depth dependency in the Manning's n formulation distributes resistance better across floodplains and captures hurricane forerunners more accurately than a constant drag coefficient (Kennedy et al., 2011; Hope et al., 2013). Another advantage is that boundary
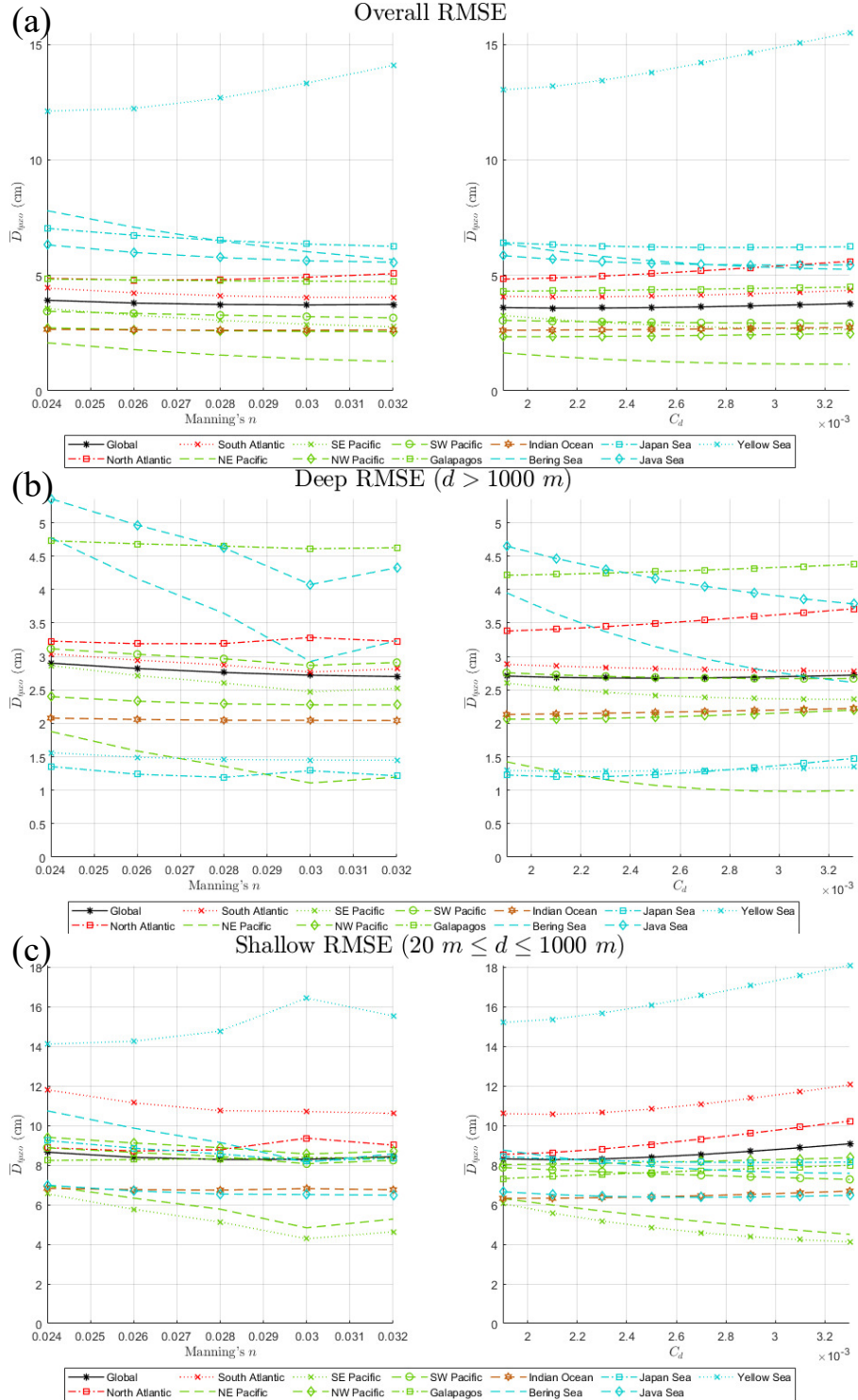
Figure 6. Comparisons of the mean discrepancy compared to TPXO9 M_2 tide as a function of varying Manning's n (on left) and constant friction coefficient (on right). (a) Overall mean discrepancy. For this study, areas shallower than 20 meters were omitted from analysis. (b) Deep mean discrepancy. Deep is defined as anything deeper than 1,000 meters. (c) Shallow mean discrepancy. Shallow is defined as anything between 20 and 1,000 meters deep.

layer dissipation in floodplains and channels is commonly parameterized using Manning's n (Arcement & Schneider, 1989). By using the same parameterization in the open ocean as in areas at risk of flooding, there is more consistency within the model.

5.2.2 Directional and Scalar C_{it}

Similar to the investigation of various bottom friction parameterization, we studied the performance of the directional and scalar forms of the internal tide parameterization by varying the tuning parameter C_{it}. Figure 7 shows the responses in mean discrepancy of the model compared to TPXO due to changing C_{it} values. As was hypothesized, the effects, especially in overall (Figure 7a) and deep water (Figure 7b) are much greater than those of altering boundary layer dissipation. Most notably, the scalar parameterization of C_{it} is highly sensitive in all basins and has a much larger impact than that of the directional parameterization. The Bering Sea especially has a large sensitivity to internal tide dissipation regardless of the parameterization used. As was discussed with regards to boundary layer dissipation, it is believed that this is due to physical processes that are not captured in our simulation due to high velocities, steep bathymetry/topography, and complex channels in the Aleutian Islands.

While the steeper curves of the scalar parameterization could result in simpler optimization, the directional model is more physically intuitive. While the scalar model has equal dissipation in all directions, the directional model only produces dissipation orthogonal to slopes. Based on the mechanisms by which internal waves are generated the directional parameterization clearly has highly desirable properties. Furthermore, the overall mean discrepancy in the directional model was lower than the overall mean discrepancy in the scalar parameterization. When studying deep and shallow regions, this pattern continues. Therefore, the directional parameterization was selected for our optimization study.

Of particular note in Figure 7 is the steepness of the curves compared to the curves in Figure 6. While bottom friction could change results by only up to a centimeter in the most drastic cases, altering C_{it} changes results by several centimeters even in the least affected regions. What is also interesting is that it appears that regions that are heavily affected by bottom friction are similarly affected by C_{it}. The Yellow Sea shows the same degradation of solution with higher C_{it} as it did with higher bottom friction coefficient. Additionally, the marginal seas exhibit much more sensitivity to friction regardless of the mechanism of dissipation. Again, we attribute this to be due to additional dissipation in those regions being required due to missed physics or simply extremely high energy dispersal over the steep island chains in those areas.

5.2.3 Global Baseline Model

Based on the above assessments, we concluded that the best methodology for examining localized sensitivity to friction—and subsequently the optimization of these localized frictional coefficients—was to select the Manning's n and directional C_{it} parameter that provided the lowest error with constant parameters when compared to TPXO9. Thus, a Manning's n of 0.028 $\mathrm{s\,m^{-1/3}}$ in the regions of high dissipation discussed in Section 5.3.1 and 0.022 $\mathrm{s\,m^{-1/3}}$ elsewhere, in combination with a C_{it} value of 2.5 with the directional parameterization were selected as baseline starting values. The mean discrepancy compared to TPXO9 of this model for the M_2 constituent was 3.70, 2.81, and 7.94 cm for an overall value, for regions deeper than 1000 meters, and for regions between 1000 and 20 meters deep respectively.
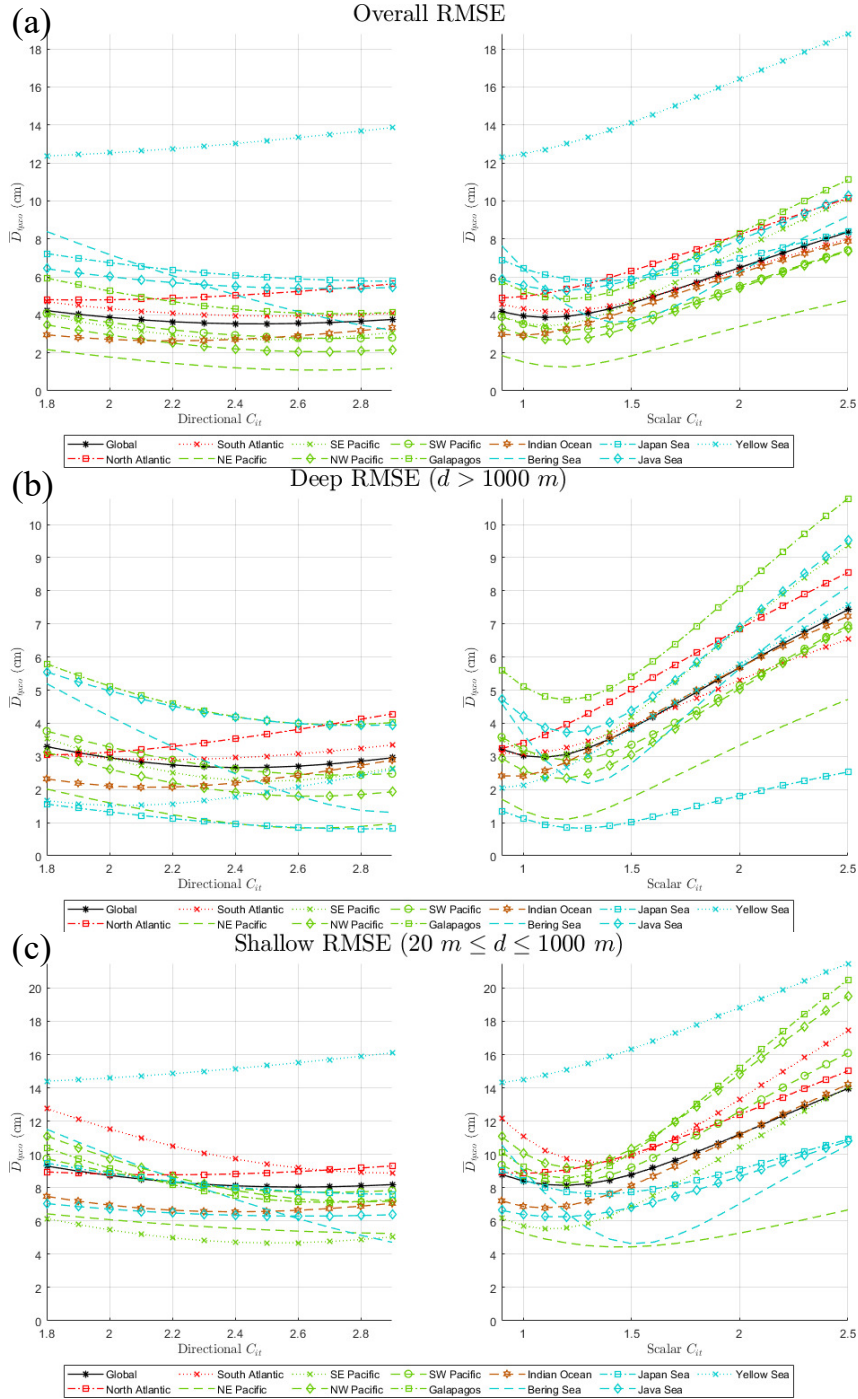
Figure 7. Comparisons of the mean discrepancy compared to TPXO9 of the M_2 tide as a function of varying C_{it} with a directional parameterization (on left) and a scalar parameterization (on right). (a) Overall mean discrepancy. For this study, areas shallower than 20 meters were omitted from analysis. (b) Deep mean discrepancy. Deep is defined as anything deeper than 1,000 meters. (c) Shallow mean discrepancy. Shallow is defined as anything between 20 and 1,000 meters deep.

5.3 Local Sensitivity to Friction Parameters

Based on the global baseline established, we further investigate areas which are particularly sensitive to local perturbations in both boundary layer and internal tide coefficients.

To facilitate these experiments, continental shelves as defined by Harris et al. (2014) were divided into 60 regions and individually had their bottom friction, in this case Manning's n, perturbed.

Unlike boundary layer dissipation, internal tide dissipation is largely concentrated in the deep ocean. It is primarily found over submerged mountain ranges, near oceanic ridges adjacent to deep trenches, and at steep continental shelf breaks. Additionally, it is not as simple to determine small regions to perturb and as such a more basin-scale approach is appropriate. Twelve individual regions were created which broadly capture unique topography and the C_{it} was perturbed using a directional parameterization.

5.3.1 Sensitivity to Bottom Friction

Bottom friction regions were selected largely based on prior experience with sensitivity, knowledge of the geomorphology of the ocean floor, and guided by the regions of high boundary layer dissipation seen in Figures 4a, 5a, 5c, and 5e. While some regions had basin scale impacts (Figure 8), the vast majority of regions perturbed showed only local changes in M_2 amplitude when the bottom friction is changed (for examples, see Figure 9). It is important to keep in context the magnitude of tidal response to perturbations of boundary layer dissipation compared to bathymetric perturbations. Note that the colorbar limits in Figure 2 are ten times those in Figures 9 and 8 (± 5 cm versus ± 0.5 cm respectively). This does not mean that regions cannot be sensitive to bottom friction, but is mentioned to reinforce the key point that bathymetry in select areas is the most influential control on global tidal results.

While most responses were either highly local (e.g., the Louisiana/Texas Shelf) or regional (e.g., the West Florida Shelf), there were several areas where basin scale responses were seen. Figure 8 shows the efect of perturbing the bottom friction in regions with particularly significant basin scale impacts, including the Hudson/Baffin Bays, George's Bank, and the European Shelf. As was hypothesized, there is a relationship between regions that are sensitive to bottom friction perturbations and regions that have high boundary layer dissipation. While it is not the case that all regions with large amounts of boundary layer dissipation are highly sensitive, it does appear that low boundary layer dissipation results in insensitivity to bottom friction.

One particularly interesting region is the George's Bank. This oval-shaped relief feature off the coast of Massachusetts is approximately 250 km long and 120 km wide, accounting for less than a tenth of a percent of the total ocean area. It is significantly shallower than the surrounding ocean and the rest of the Massachusetts Bay, with depths ranging from approximately 15 to 70 meters. As Figure 4a shows, George's Bank has very high boundary layer dissipation owing to its shallow depths, high velocity flows, and rough and scoured sediments. Changing the bottom friction on the George's Bank affects the M_2 amplitude all along the east coast of the United States, in the west Caribbean, and even off the coasts of Brazil and in the Gulf of Guinea as seen in Figure 8c. While some other regions have similar extent of response to perturbations, all of them are significantly larger in area than George's Bank.

Most areas with this high sensitivity have a number of things in common. Foremost among these are high dissipation rates. Egbert and Ray (2001) provides a list of the largest tidal dissipators based on calculations from data assimilated tidal models. While the regions used in their calculations are not identical to those used in this study, there is significant overlap in what they found to be the largest tidal dissipators and regions found to be highly sensitive to bottom friction in this study. For example, Egbert and Ray (2001) found that the largest shallow water tidal dissipator was the Hudson Bay (in their study, the Hudson Bay region also included Baffin Bay, the Labrador Sea, and the
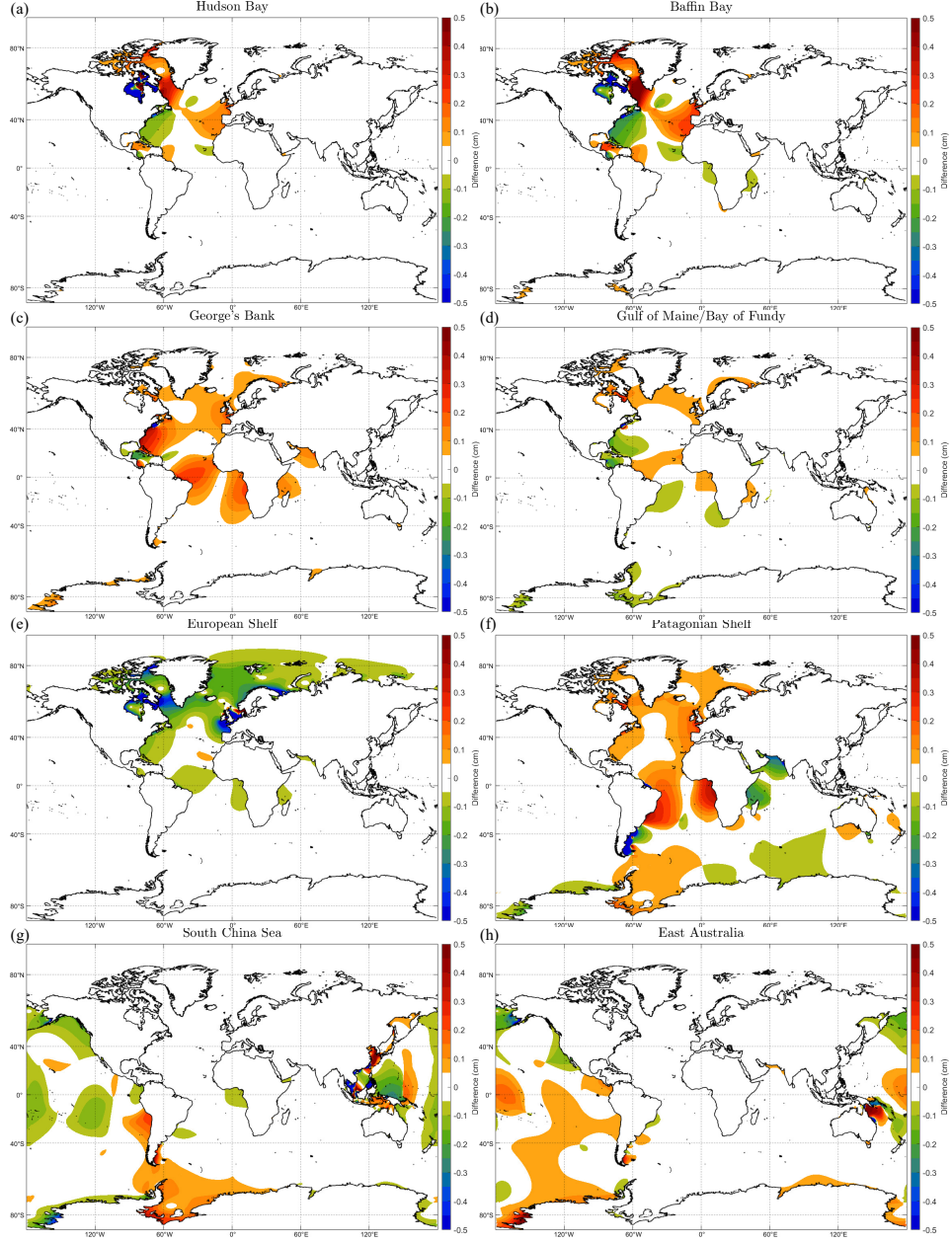
Figure 8. Examples of basin-scale responses in the M_2 amplitude due to perturbing Manning's n by $0.002 \ \mathrm{s\,m^{-1/3}}$ in certain regions.
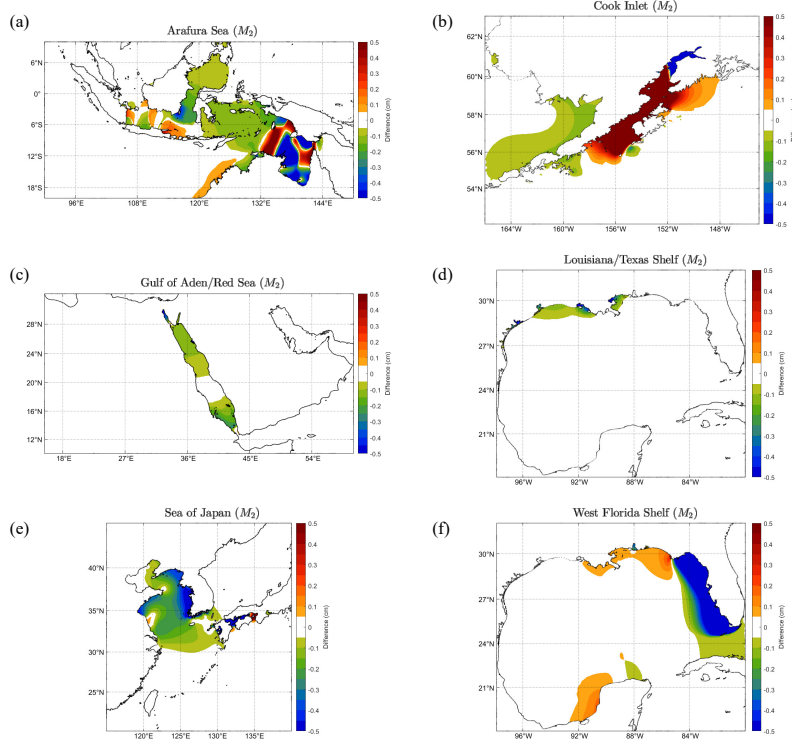
Figure 9. Response of the M_2 amplitude to raising the Manning's n by $0.002\ \mathrm{s\,m}^{-1/3}$ in selected regions. (c) and (d) are examples of highly local responses, i.e., the response is confined almost entirely to the region with perturbed friction. (a), (b), (e), and (f) show region-scale responses, with responses not necessarily confined to the region with perturbed friction but not nearly on a basin-scale.

Northwest Passage). In this study, two of the largest responses to perturbing Manning's n are seen in Baffin Bay (Figure 8b) and the Hudson Bay (8f). Raising the friction in these two regions has an effect throughout the North Atlantic, lowering tides along the east coast of the United States and raising them in Western Europe and North Africa.

Another region known to be a large tidal dissipator is the European Shelf. Again, the response to raising friction within this highly dissipative area is highly non-local. Figure 8d shows how altering friction within the European Shelf altered the M_2 tide throughout the North Sea, the North Atlantic, and even within the Gulf of Guinea and the northern Mozambique Channel. The Patagonian Shelf (8g), Eastern Australia (8c), and the Bay of Fundy (8e) also make both the list of large tidal dissipators and highly sensitive regions.

In most cases, tidal responses to altering bottom friction within a region are completely local, i.e., varying friction only changes results within the region of altered friction. Figures 9c and 9d show two examples of this. In the majority of cases, these highly local responses are in regions with relatively low tidal velocities and are often within larger bays or inlet systems. These types of perturbation responses are often very small in magnitude, with magnitudes only up to 0.2 cm or so.

Another common response seen was a "regional" response. For example, Figure 9f shows the response of the tides to raising friction on the West Florida Shelf. In this case, there is a noticeable response outside the shelf in question, with a response on the west and north sides of the Yucatan Peninsula as well as some change in the Straits of Florida. Unlike the Louisiana/Texas shelf (9d) and the Gulf of Aden/Red Sea (9d), the West Florida shelf experiences relatively high tidal velocities. By altering the dissipation within that region, the dynamics within the Gulf of Mexico are thus changed, altering the tidal response within the localized basin. Similar responses can be seen in Cook Inlet (9b), which has a large tidal range and is a key dissipator in Alaska, resulting in perturbation responses within Bristol Bay and the Shelikof Strait; the Arafura Sea (9a), which is surrounded by complex island systems and channels, resulting in high velocities and large responses throughout the Java Sea, Gulf of Carpentaria, and even extending up to the Sulu Sea and the West Australian Shelf; and the Sea of Japan (9e), where raising the friction in the Taiwan Strait results in a large response within the Yellow Sea. This is not a comprehensive list of regional or highly local responses, but rather gives examples of some regions where such responses can be seen.

Because there are a limited number of regions which have large scale effects when their bottom friction is changed, we decided to consider only select regions for their bottom friction in the optimization. This decision was made for two reasons. The first reason was computation and time efficiency. With 60 regions to perturb and then optimize, the amount of time and computer resources used would be disproportionate to the expected improvement in tidal results. The second, and perhaps more important, reason was that most regions are largely insensitive to bottom friction. While local results might improve by changing bottom friction in, for example, the Puget Sound, it would have little to no effect globally. As such, regions that were highly sensitive, as well as a few that are of interest for future work, were selected. These regions are listed in Table 2. Figure 10 shows the geographical extent of the selected regions.

5.3.2 Sensitivity to Coefficient of Internal Tides

Similarly to establishing regions for Manning perturbations, selecting regions for C_{it} was performed largely on prior experience with global models. To a large degree regions were selected to encompass unique areas of steep bathymetric gradient, e.g., breaking out the Galapagos region to contain the large submerged mountains in that area. Figure 11 shows the geographic extent of these regions. Other regions were defined due to prior experience with optimizing C_{it} values. For example, splitting up the Atlantic Ocean in to north and south regions was performed because prior models have benefited from having separate values in these two regions. Additionally, by using smaller regions, there
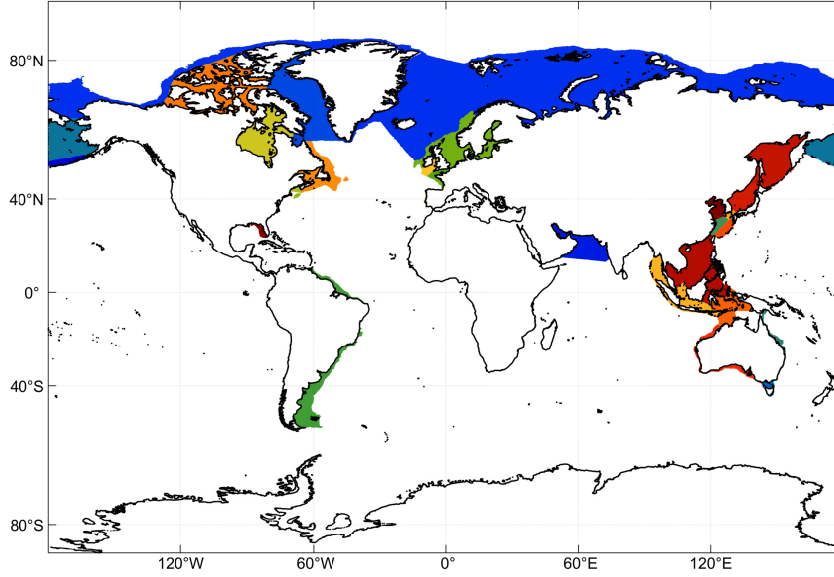
Figure 10. Boundary layer dissipation regions selected for use in the global optimization. Most areas were chosen due to the basin-scale response to frictional perturbation. Some—including the West Florida Shelf and the Gulf of St. Lawrence—were selected due to future work focused on those areas.

are more degrees of freedom in the optimization and thus a greater ability to optimize the model. Each defined region tried to characterize broadly the physical character of that portion of the basin.

The Pacific was broken up largely to be consistent with the Atlantic as well as due to the large geographic extent of the Pacific Ocean. Historically, our global models have had major differences with data assimilated tidal models as TPXO9 in the Galapagos, for this reason, and the aforementioned submerged mountains in the area, the Galapagos was given its own region.

The remaining regions, including the Bering Sea, Sea of Ohkotsk, Yellow Sea, and Java Sea regions were selected due to the steep bathymetric gradients and large island chains in those regions. While the magnitudes of response to the perturbations of C_{it} are similar to those due to perturbing Manning's n (and are still significantly lower in magnitude than sensitivity to bathymetry), the geographic extent is far more wide reaching.

Figure 12 shows the responses to all twelve regions that were used. With the exceptions of the Bering Sea (12j), the Japan and Ohkotsk Seas, and the East China/Yellow Sea, all of the C_{it} regions had responses to the perturbation that were more far reaching than even the most non-local Manning perturbation. More importantly, there is significant overlap between the response in, for example, the response to perturbing C_{it} in the North Atlantic and the response to perturbing C_{it} in the South Atlantic. Clearly, the optimization of internal tide coefficients is a coupled problem.

There are a number of intriguing observations to be made about the responses to altered internal tide friction seen in Figure 12. First, there is notable similarity between the sensitivity in the North Atlantic (12a) and South Atlantic (12b). While the South Atlantic has more of an effect outside of the Atlantic Basin, especially in the Indian Ocean and along the West Coast of the Americas, within the Atlantic there is remarkable consistency. Additionally, within the Pacific Ocean, the Southwest (12e) and Northeast (12d) perturbations seem to have had a larger effect than the Southeast (12f) and Northwest
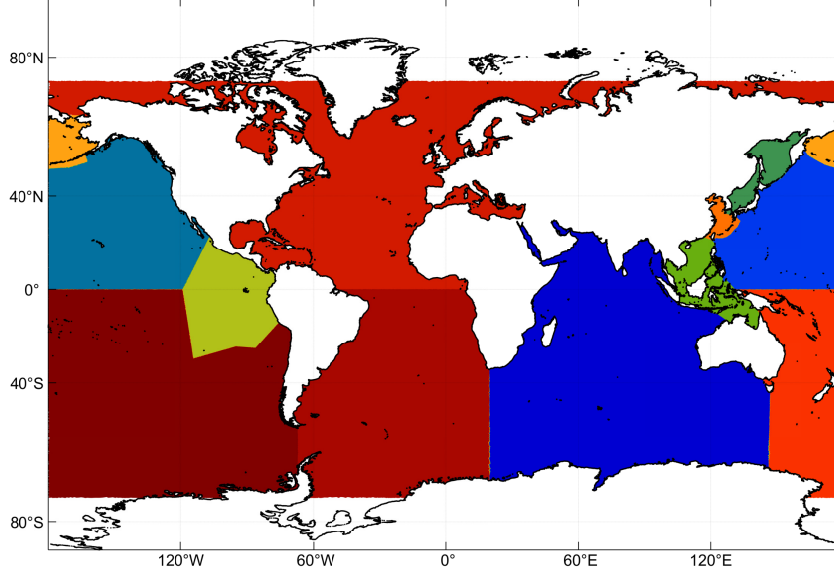
Figure 11. C_{it} regions used for optimization. A full list of region names can be found in Table 3. An important note is that NE Pacific is the region bound in the south by the equator, in the east by the prime meridian, and on the north and west by the Bering, Ohkotsk, Japan, and South China Seas. Similarly the SE Pacific is south of the equator, west of the prime meridian, and east of the Indian Ocean. NW Pacific is north of the equator, east of the prime meridian, and west of the west coast of North America. SW Pacific is south of the equator, east of the prime meridian, and west of South America.

(12c). While the magnitude of responses were different, the areas affected were quite similar. Additionally, the Galapagos region (12g) has an extremely large effect.

While the Bering Sea, Japan and Ohkotsk Seas, and the East China/Yellow Sea all had largely local effects, they were included as separate regions despite their relative insensitivity globally mainly because of our experiences of poor results within those regions. The hope was that by optimizing the C_{it} within them separately, results could be improved due to extra degrees of freedom and capturing local physics. Note that the lack of regions in the far north and south of the globe is due to the parameterization of internal tide being undefined in those latitudes.

6 Global Optimization

6.1 Optimization of parameters

In order to optimize both the internal tide and Manning's n parameters, it is useful to treat the complex amplitude at a point in the model as the baseline complex amplitude plus the changes in amplitude due to the alteration of friction factors in various locations. This allows for relative simplicity in predicting what tidal results will be without performing hundreds of tidal simulations as well as accounting for both the amplitude and phase to be optimized simultaneously. We will use the following definitions:

$$Z_{o,m}^k = Re_{o,m}^k + iIm_{o,m}^k \tag{15}$$

$$Z_{b,m}^k = Re_{b,m}^k + iIm_{b,m}^k \tag{16}$$

$$f_m^k(\boldsymbol{x}) = g_m^k(\boldsymbol{x}) + ih_m^k(\boldsymbol{x}) \tag{17}$$
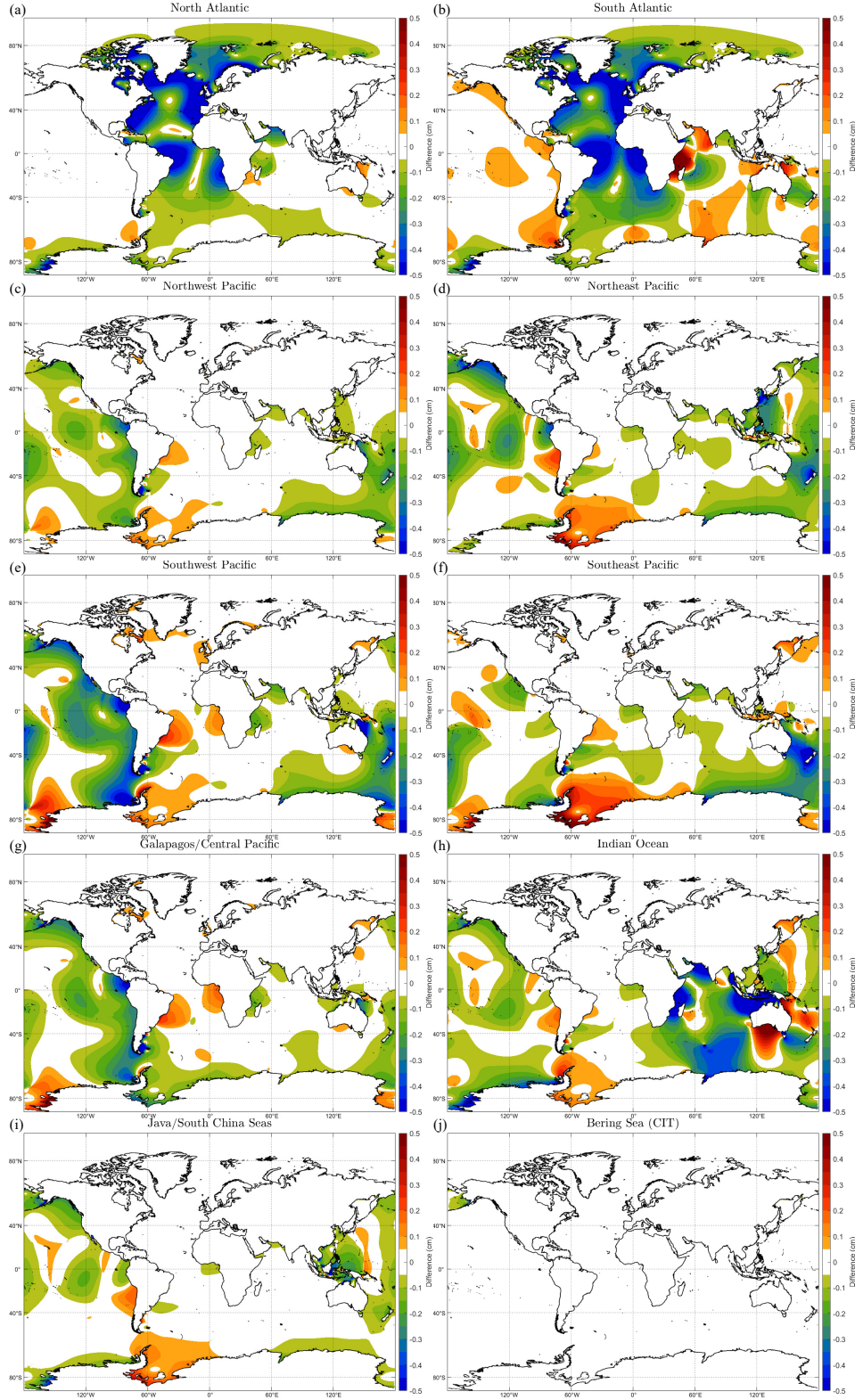
Figure 12. Responses in M_2 amplitude to perturbing C_{it} by 0.2 within certain regions. Note that most show heavily non-local effects. Also note the overlap in responses especially between regions in the same oceans. Japan/Ohkotsk Seas and East China/Yellow Seas regions were omitted because they showed only local effects.

754   where $Z_{o,m}^k$ is the observed complex amplitude composed of real (Re) and imaginary (Im)
755   parts interpolated from TPXO9 of constituent k at centroid m and i denotes the imag-
756   inary unit ($i^2 = -1$). Similarly, $Z_{b,m}^k$ is the complex amplitude of constituent k at node
757   m in the baseline run from which the perturbations are made, $f_m^k(\boldsymbol{x})$ is the complex val-
758   ued real function that describes the changes in complex amplitude of constituent k at
759   node m as a function of the change in friction factor vector $\boldsymbol{x}$ in the M regions of inter-
760   est. f_m^k is further decomposed into the real valued functions $g_m^k(\boldsymbol{x})$ and $h_m^k(\boldsymbol{x})$. Both g_m^k
761   and h_m^k can be written as the summation of functions $g_{j,m}^k(x_j)$ and $h_{j,m}^k(x_j)$, which are
762   the changes at node m of the kth constituent of the real and imaginary components due
763   the altering friction in region j. This results in:

$$g_m^k(\boldsymbol{x}) = \sum_{j=1}^{M} g_{j,m}^k(x_j) \tag{18}$$

$$h_m^k(\boldsymbol{x}) = \sum_{j=1}^{M} h_{j,m}^k(x_j) \tag{19}$$

764   With (8)-(12), the so-called cost function can be defined as the absolute value of the dif-
765   ference between the observed and modelled complex amplitudes–where the modelled am-
766   plitude is $Z_{m,i}^k = Z_{b,i}^k + f_i^k(\boldsymbol{x})$:

$$E_i^k(\boldsymbol{x}) = \sqrt{(Z_{o,i}^k - Z_{b,i}^k - f_i^k)(Z_{o,i}^k - Z_{b,i}^k - f_i^k)^*}$$

$$E_i^k(\boldsymbol{x}) = ([(Re_{o,i}^k - Re_{b,i}^k - g_i^k(\boldsymbol{x})) + i(Im_{o,i}^k - Im_{b,i}^k - h_i^k(\boldsymbol{x}))]* \tag{20}$$

$$[(Re_{o,i}^k - Re_{b,i}^k - g_i^k(\boldsymbol{x})) - i(Im_{o,i}^k - Im_{b,i}^k - h_i^k(\boldsymbol{x}))])^{\frac{1}{2}}$$

$$E_i^k(\boldsymbol{x}) = ((Re_{o,i}^k - Re_{b,i}^k - g_i^k(\boldsymbol{x}))^2 + (Im_{o,i}^k - Im_{b,i}^k - h_i^k(\boldsymbol{x}))^2)^{\frac{1}{2}} \tag{21}$$

767   The above cost function is a measure of the error at node i of constituent k. To create
768   a global cost function, sum over all the constituents $k = 1$ to L and all the elements
769   $i = 1$ to N:

$$E(\boldsymbol{x}) = \sum_{i=1}^{N} \sum_{k=1}^{L} E_i^k(\boldsymbol{x}) \tag{22}$$

770   Expand $g_i^k(\boldsymbol{x})$ and $h_i^k(\boldsymbol{x})$ as Taylor series and linearize:

$$g_i^k(\boldsymbol{x}) \approx g_i^k|_{\boldsymbol{x_0}} + \nabla g_i^k|_{\boldsymbol{x_0}}(\boldsymbol{x} - \boldsymbol{x_0}) \tag{23}$$

$$h_i^k(\boldsymbol{x}) \approx h_i^k|_{\boldsymbol{x_0}} + \nabla h_i^k|_{\boldsymbol{x_0}}(\boldsymbol{x} - \boldsymbol{x_0}) \tag{24}$$

771   Finally, let $\boldsymbol{x_0} = 0$ and the cost function becomes:

$$E(\boldsymbol{x}) = \left[\sum_{i=1}^{N} \sum_{k=1}^{L} \left((Re_{o,i}^k - Re_{b,i}^k - \nabla g_i^k|_{\boldsymbol{x_0}} \boldsymbol{x})^2 + (Im_{o,i}^k - Im_{b,i}^k - \nabla h_i^k|_{\boldsymbol{x_0}} \boldsymbol{x})^2 \right)^{\frac{1}{2}} \right] \tag{25}$$

772   Given all of the perturbations from Section 5 and this cost function, it is possible
773   to find the combination of parameters for the 41 regions of interest (12 C_{it} and 29 Man-
774   ning) that will minimize the error in the domain. For this study, MATLAB's fmincon
775   function was used, which utilizes an interior point algorithm to find the minimum of a
776   multi-dimensional function within certain constraints (MATLAB, 2018). Initially, lim-
777   its were set to accepted ranges of values, with C_{it} being allowed to range between 1.0
778   and 4.0 and Manning values to range between 0.018 and 0.050. The purpose of these lim-
779   its was to both ensure convergence to an optimum and also to keep values relatively close
780   to those tested as global values as discussed in Section 5.2.

6.2 Optimized Parameters

782   The optimization of frictional parameters occurred in two parts. First, comparing
783   to TPXO9, the M_2 amplitude at the centroid of all elements in the mesh with bathy-

Table 2. Manning's n ($s\,m^{-1/3}$) for regions of interest for progression of runs. Asterisks denote regions that, following the global optimization, were re-optimized locally. Numbers denote regions that were sub-divided following the global optimization.

Region	Global Baseline	Global Optimization	Local Re-Optimization
Aleutian Islands*1	0.028	0.037	0.087
Arabian Sea/Persian Gulf	0.028	0.018	0.021
Arctic Ocean	0.028	0.042	0.042
Baffin Bay	0.028	0.027	0.027
Bass Strait	0.028	0.018	0.025
Bering Sea*1	0.028	0.037	0.025
East Australian Shelf	0.028	0.018	0.018
East China Sea*2	0.028	0.026	0.010
English Channel*3	0.028	0.033	0.026
European Shelf*3	0.028	0.033	0.026
George's Bank	0.028	0.033	0.033
Gulf of Maine/Bay of Fundy	0.028	0.035	0.035
Gulf of St. Lawrence	0.022	0.018	0.018
Hudson Bay	0.028	0.029	0.029
Irish Sea*3	0.028	0.033	0.026
Java Sea/Gulf of Thailand	0.028	0.041	0.036
Korean Strait*2	0.022	0.022	0.015
Northwest Passage	0.028	0.048	0.048
North Australian Shelf	0.028	0.023	0.023
Patagonian Shelf*	0.028	0.025	0.031
Ryuku Islands*2	0.028	0.026	0.099
Salish Sea*4	0.022	0.022	0.022
Sea of Japan*2	0.022	0.022	0.046
Sea of Ohkotsk	0.028	0.030	0.030
South China Sea	0.028	0.041	0.040
Southwest Australian Shelf	0.028	0.023	0.023
Strait of Georgia/Puget Sound*4	0.022	0.022	0.022
West Florida	0.022	0.029	0.034
Yellow Sea	0.028	0.023	0.020

metric depth greater than 20 meters were considered. The cost function above was calculated at each of these centroids for only the M_2 constituent, because it dominates the tides in most locations. Following this global optimization of local parameters, there were some shelf regions that had large errors. For example, the European shelf region had significant underprediction as seen in the global difference between the globally optimized run and TPXO9 (Figures 13e and 13f). To further reduce these errors, the cost function minimization was locally reapplied to optimize the Manning's n within that region. This was applied selectively in areas that had particularly bad solutions and was only done for Manning's n. In these local re-optimizations, areas with particularly high error such as the European Shelf were subdivided into smaller regions (Irish Sea, English Channel, and European Shelf), individually perturbed once more, and the cost function minimization was re-applied only within the European shelf. While these local re-optimizations somewhat degraded deep ocean results globally, the shallow water solutions improved drastically, especially in the regions in which this treatment was used (Figure 13g and 13h). Tables 2 and 3 summarize the optimized coefficients.

6.2.1 Manning's n

An important factor in examining the results of this optimization is to attempt to examine what Manning's n one would find in the regions of interest using conventional methods. The selection of Manning's n coefficients is highly dependent on in situ conditions. While initially created for use in open channel flow, it has been adapted to floodplain and open ocean use. Factors that affect the selection of Manning's n coefficients
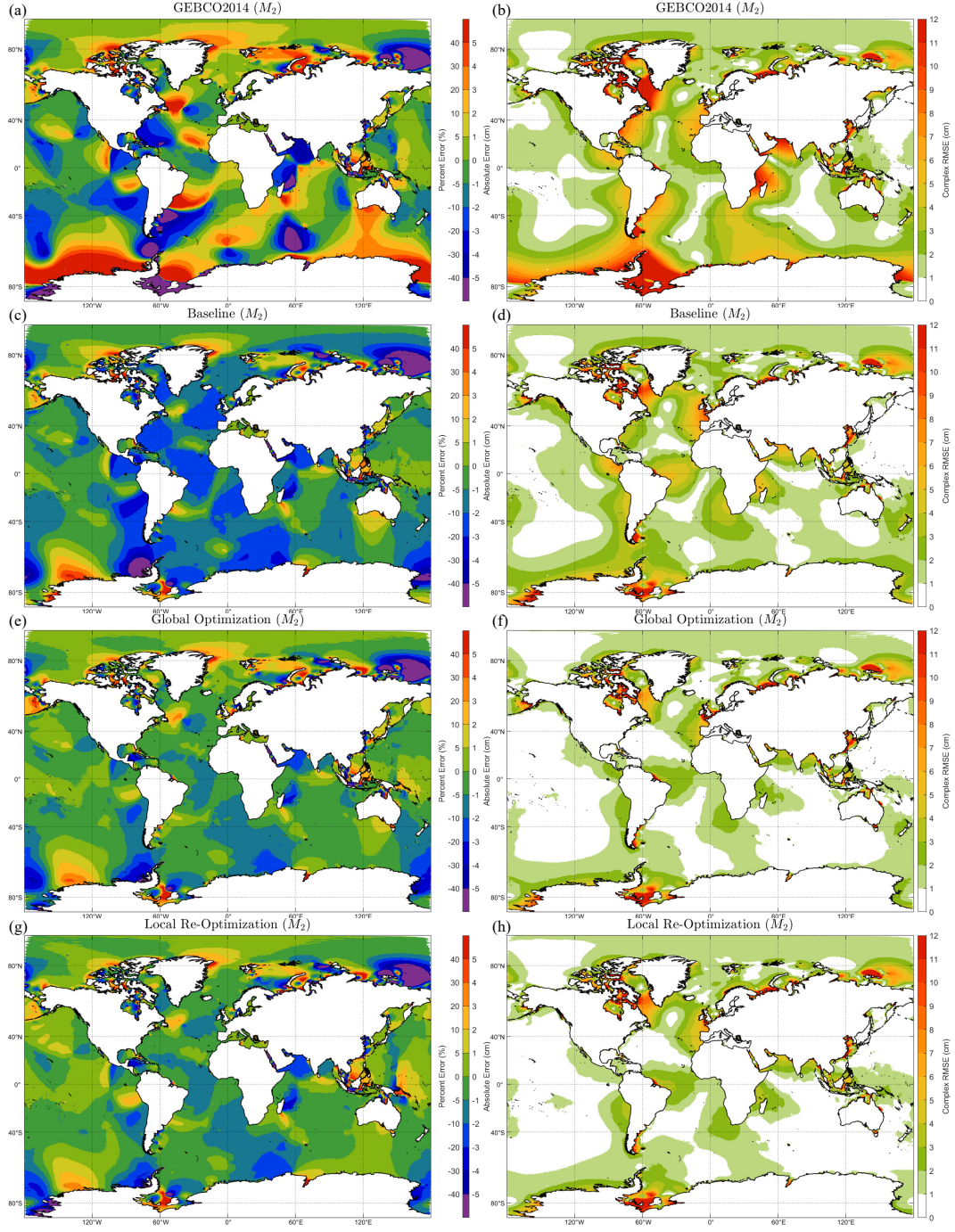
Figure 13. Progression of error from Global Baseline, to First Global Optimization, to Local Re-Optimization. Figures on left show amplitude error compared to TPXO9 based on error brackets as seen in the colorbar with the minimum bracket of either percentage or absolute error being displayed. This allows for accurate representations of error to be displayed. For instance, at amphridromic points, a small absolute error produces a large percentage error and hence the solution appears worse than it is. Figures on right show the complex error (in this case mean discrepancy from TPXO9).

include roughness of sediments in a region, the amount of scouring/dunes/bedform roughness, and the presence of any obstructions/vegetation. Unfortunately, it is quite difficult to find accurate Manning values for different regions of the open ocean due to lack of knowledge of the ocean bottom. In the past, attempts have been made to estimate friction factors based on paramaterized estimates of roughness, substrate, and current speed (Pringle et al., 2018a). However, as can be seen in Table 2 and discussions below, it is possible to achieve physically consistent values through the use of an optimization metric such as the one described in this paper.

One observation that springs out when examining Table 2 in conjunction with Figure 4a is that most of the high energy areas tend towards a Manning's n of ≈ 0.028 s m$^{-1/3}$. Such areas include Baffin Bay (0.027 s m$^{-1/3}$), the Bass Strait (0.025 s m$^{-1/3}$), the English Channel (0.026 s m$^{-1/3}$), the European Shelf (0.026 s m$^{-1/3}$), George's Bank (0.033 s m$^{-1/3}$), the Gulf of Maine (0.035 s m$^{-1/3}$) and Hudson Bay (0.029 s m$^{-1/3}$). All of these regions were identified as having very high dissipation rates. The reason for these consistent values of Manning's n is that the high velocity currents in these regions will strip away fine sediments, create large ripples and dunes on the seabed, and create a rougher surface that results in higher Manning's n than the typical 0.022 s m$^{-1/3}$.

One important qualifier to this trend is the case of the Aleutian and Ryuku Islands. When setting the upper limit to 0.050 s m$^{-1/3}$ for optimized Manning values, there was still a huge over prediction throughout the Bering Sea and Shelf as well as within the Korean Strait and Yellow Sea. Due to past experience, it was thought that this was due to lack of capturing some dissipation mechanism through the Aleutian Islands through lateral and vertical eddying. High velocity flows and the presence of eddying also increase turbulence, increasing the boundary layer dissipation which would require a higher Manning's n to capture. In order to capture some of this dissipation without sacrificing accuracy in other regions, the Aleutian and Ryuku islands were separated from their respective regions (Bering and East China Seas respectively) and the upper limit on Manning's n was removed. The new optimized value for Manning became 0.087 s m$^{-1/3}$ for the Aleutians, which is high, but still physically reasonable, and was capped at 0.099 s m$^{-1/3}$ for the Ryuku Islands lest it degrade results. For the most part, the other values did not require being on the boundary to produce a minimum, and so the bounds did not pose a problem. Additionally, several regions which past studies have shown to require low friction, such as the Yellow Sea, require lower than the widely used value of 0.022 s m$^{-1/3}$ (Pringle et al., 2018a). While the Yellow Sea does dissipate a large amount of tidal energy (see Figure 4a), this marginal sea is characterized by fine sediments deposited by rivers that flow into it. These sediments result in a lower than usual Manning's n. Another interesting note is the optimal value for the Arctic Ocean and Northwest Passage. These regions have Manning values of 0.042 and 0.048 s m$^{-1/3}$ respectively, higher than most of the highly dissipative regions. We posit that this higher friction is due to the presence of sea ice in those regions, which creates two interfaces of boundary layer friction—the bottom of the ocean and the bottom of the ice shelf.

In addition to the global optimization performed here, we showed through the local re-optimizations of the European Shelf, the Yellow/East China/Japan Seas, and the Puget Sound/Strait of Georgia that this methodology could be used to locally improve friction parameters in regions of interest, e.g., applying a local optimization to the Gulf of Mexico region for hurricane prediction.

6.2.2 Coefficient of Internal Tides

Establishing a physical basis for the selection of C_{it} values is much harder than for Manning's n. This is largely due to the resolution-dependence of this parameter. This appears to be supported by the optimized values seen in Table 3. As with Manning's n, the Bering Sea (which contains the Aleutian Islands) has capped out at the maximum value allowed. This is again believed to be due to unresolved physics due to missing some sort of dissipation.

Another region of interest is the area surrounding the Galapagos Islands off the western coast of Central America. When the same values used in the greater Pacific Ocean, this entire region is largely under predicted. After separating the various regions of the Pacific, the Galapagos region improves drastically. What is intriguing is that, as seen in Table 3, all of the Pacific regions except the SW Pacific have C_{it} values that are quite high. Examining Figure 12e, it is easy to see that the M_2 amplitude in the Galapagos region is heavily controlled by the SW Pacific. When C_{it} was raised in the SW Pacific, the Galapagos region had a decreased tidal amplitude. Thus, lowering C_{it} in the SW Pacific will raise the amplitude in the Galapagos. It appears that any decrease in the M_2 amplitude due to raising C_{it} in the NW, NE, and SE Pacific—as well as in the Galapagos region itself—is counteracted by the lower value used in the SW Pacific.

The Atlantic basin in the Global Baseline is very under-predicted as seen in Figure 13c. As the sensitivity plots for the North and South Atlantic (Figures 12a and 12b respectively) indicate, lowering C_{it} in those regions will raise the M_2 amplitude. This expectation is born out in Table 3, where it can be seen that the optimal C_{it} values for the North and South Atlantic are 2.2 and 1.0 respectively.

Attempts were made to find some relationship between the optimal C_{it} values and the magnitude of the slopes in each region. Unfortunately, there did not appear to be a clear correlation between the two values. Additionally, when an attempt to re-perturb and re-optimize C_{it} was performed, the friction factors did not converge to values consistent with the first global optimization.

We believe there are several reasons that the C_{it} does not optimize as neatly as boundary layer dissipation. First, the parameterization of internal tide conversion is somewhat mesh and resolution-dependent. While the topographic length scale parameter does a good job placing resolution in areas of high bathymetric gradient, it cannot place minimum resolution in all those places. Second, unlike Manning's n, there is large variability in the value of C_{it} that is optimal for a region. Because of this, the starting point ($C_{it} = 2.5$) for the optimization metric was far away from the optimal value for regions with very high or very low optimal values. The optimization algorithm uses a linearization of the response function of amplitude to changing frictional value and thus may not be ideal for this application. This hypothesis is supported by Figures 6 and 7. The slopes of the error function as a function of changed frictional coefficient are far steeper for C_{it} than they are for boundary layer dissipation. As a proxy for the response in the tidal amplitude, the mean discrepancy compared to TPXO, $\bar{D}_{tpxo}$ (see equation 8) highlights that changing C_{it} has a larger effect than changing Manning's n. Finally, the global nature of the response of the tides to perturbations in internal tide dissipation means that there may be more than one optimal set of coefficients, which could cause inconsistencies between the slopes and the values of C_{it}.

In addition to the challenges inherent in our optimization technique, there are exterior factors that affect the optimal C_{it} values. Foremost among these is the complexity of the baroclinic to barotropic conversion phenomenon. While internal tide dissipation has been studied for decades (Garrett & Kunze, 2007), there is uncertainty in the best method to parameterize this complicated process. Additionally, the use of decadally averaged salinity and temperature fields from observational data could result in imperfect depth-averaged values. Despite these challenges, there can be no doubt that this optimization scheme greatly improved tidal results in this model both in the deep ocean and in coastal areas.

7 Summary and Discussion

The simplest method to evaluate the effects of the optimization is to examine the global error metrics as seen in Table 4. First, let us consider the comparisons to TPXO9 since that is the reference solution used in the cost function. In the overall mean discrepancy from TPXO, there is an improvement from the global baseline to the global optimization of almost 0.6 centimeters in the M_2 constituent. The additional improvement

Table 3. Optimized C_{it} values

Region	Optimal C_{it}
North Atlantic	2.2
South Atlantic	1.0
Bering Sea	2.4
NE Pacific	3.4
SE Pacific	4.0
NW Pacific	4.0
SW Pacific	1.7
Galapagos	4.0
Indian Ocean	1.4
Japan Sea	3.8
Java Sea	1.0
Yellow Sea	1.2

seen in the local re-optimization is almost negligible in the overall statistics. In the deep ocean, the global optimization improves the results by over a centimeter. Unfortunately this improvement is to the detriment of the shallow solution, where results actually got worse in the global optimization. As has already been mentioned, the use of the local reoptimization improves the shallow solution compared to TPXO by 0.36 centimeters for the M_2 over the global optimization (a net improvement from the global baseline of 0.2 centimeters). At the same time, the deep water solution degrades slightly; however, it is still a net improvement of 0.86 centimeters.

When comparing to the measured station data, the results are even more interesting. Noting that the stations were not included in the cost function, there is a marked improvement. Deep station results improve in the same pattern as when comparing to TPXO9, i.e. improving for the global optimization then degrading slightly with the local optimization. The shallow station also show the same pattern as their counterparts in TPXO9. Where the trends become most interesting is when comparing to coastal stations. Because areas less than 20 meters in depth were omitted from the TPXO9 cost function, there is no analogous error metric for the coastal stations to compare with TPXO9. However, where the coastal stations differ from the shallow stations is in improvement over both steps of the optimization. With a net improvement of 1.11 centimeters, the shallow station error metric is where the most global improvement is seen.

We believe that the shallow water solutions not improving with the global optimization is due to the error function minimization sacrificing shallow areas in an attempt to improve the deep ocean. One specific example is the European Shelf. By raising the friction on the shelf, the North Atlantic, which is very under predicted in the baseline run, sees an increase in the M_2 amplitude. Hence, the error minimization tries to raise that friction in order to improve the North Atlantic to the detriment of the solution on the European Shelf. However, by performing the local re-optimization, this is corrected and the shallow results see a net improvement.

For constituents other than the M_2, there is, generally, improvement for semi-diurnal constituents. Despite not being included in the cost function, the S_2, N_2, and K_2 all show improvement in most error metrics (the exceptions being the mean discrepancy compared to stations in shallow regions for the S_2 and K_2). The diurnal constituents, on the other hand largely stayed the same or degraded slightly overall. While select error metrics for the diurnal constituents did show modest improvement, there is not an obvious trend. Importantly, the 8 constituent error metrics all improved.

Figure 13 also highlights the improvements compared to TPXO9 and shows that in certain basins they are far better than the global error metric indicates. The under-

Table 4. Summary of error statistics for major eight constituents for Baseline, Globally Optimized, and Locally Re-Optimized runs. All error metrics are given in centimeters.

Const.	Error Metric	Global Baseline	Global Optimization	Local Re-Optimization
8 Const	$\bar{D}_{tpxo,overall}$	5.18	4.61	4.59
	$\bar{D}_{tpxo,deep}$	3.94	3.03	3.11
	$\bar{D}_{tpxo,shallow}$	11.15	11.18	10.90
	$\bar{D}_{sta,deep}$	3.75	3.04	3.18
	$\bar{D}_{sta,shallow}$	10.18	13.74	9.77
	$\bar{D}_{sta,coast}$	9.67	9.26	8.85
M_2	$\bar{D}_{tpxo,overall}$	3.70	3.10	3.10
	$\bar{D}_{tpxo,deep}$	2.81	1.77	1.94
	$\bar{D}_{tpxo,shallow}$	7.96	8.10	7.74
	$\bar{D}_{sta,deep}$	2.67	1.72	1.94
	$\bar{D}_{sta,shallow}$	7.18	9.52	6.16
	$\bar{D}_{sta,coast}$	6.47	6.02	5.63
S_2	$\bar{D}_{tpxo,overall}$	2.83	2.49	2.45
	$\bar{D}_{tpxo,deep}$	2.37	2.09	2.03
	$\bar{D}_{tpxo,shallow}$	5.34	4.72	4.71
	$\bar{D}_{sta,deep}$	2.41	2.19	2.19
	$\bar{D}_{sta,shallow}$	4.93	6.12	5.12
	$\bar{D}_{sta,coast}$	4.27	4.09	4.17
N_2	$\bar{D}_{tpxo,overall}$	0.77	0.70	0.72
	$\bar{D}_{tpxo,deep}$	0.56	0.39	0.43
	$\bar{D}_{tpxo,shallow}$	1.75	1.83	1.85
	$\bar{D}_{sta,deep}$	0.51	0.38	0.43
	$\bar{D}_{sta,shallow}$	1.76	2.02	1.64
	$\bar{D}_{sta,coast}$	1.40	1.33	1.32
K_2	$\bar{D}_{tpxo,overall}$	0.90	0.47	0.48
	$\bar{D}_{tpxo,deep}$	0.59	0.32	0.32
	$\bar{D}_{tpxo,shallow}$	2.20	1.13	1.14
	$\bar{D}_{sta,deep}$	0.41	0.36	0.36
	$\bar{D}_{sta,shallow}$	1.01	1.37	1.03
	$\bar{D}_{sta,coast}$	1.14	1.09	1.04
K_1	$\bar{D}_{tpxo,overall}$	1.67	1.83	1.83
	$\bar{D}_{tpxo,deep}$	1.01	1.05	1.06
	$\bar{D}_{tpxo,shallow}$	4.26	4.78	4.76
	$\bar{D}_{sta,deep}$	0.54	0.73	0.74
	$\bar{D}_{sta,shallow}$	1.84	1.99	1.80
	$\bar{D}_{sta,coast}$	1.71	1.87	2.00
O_1	$\bar{D}_{tpxo,overall}$	0.78	1.00	1.00
	$\bar{D}_{tpxo,deep}$	0.44	0.51	0.54
	$\bar{D}_{tpxo,shallow}$	2.06	2.73	2.67
	$\bar{D}_{sta,deep}$	0.28	0.34	0.38
	$\bar{D}_{sta,shallow}$	1.00	1.35	1.04
	$\bar{D}_{sta,coast}$	1.10	1.17	1.29
P_1	$\bar{D}_{tpxo,overall}$	0.53	0.51	0.52
	$\bar{D}_{tpxo,deep}$	0.32	0.23	0.28
	$\bar{D}_{tpxo,shallow}$	1.34	1.36	1.38
	$\bar{D}_{sta,deep}$	0.18	0.19	0.20
	$\bar{D}_{sta,shallow}$	0.65	0.66	0.67
	$\bar{D}_{sta,coast}$	0.64	0.68	0.70
Q_1	$\bar{D}_{tpxo,overall}$	0.18	0.21	0.21
	$\bar{D}_{tpxo,deep}$	0.12	0.12	0.13
	$\bar{D}_{tpxo,shallow}$	0.44	0.53	0.54
	$\bar{D}_{sta,deep}$	0.18	0.18	0.17
	$\bar{D}_{sta,shallow}$	0.71	0.68	0.67
	$\bar{D}_{sta,coast}$	0.33	0.33	0.35

prediction throughout the Atlantic Ocean is largely solved and much of the Pacific Ocean has also improved. Figure 13a and 13b are included to again highlight the magnitude of improvement that can be seen by using higher quality bathymetry over and above any improvement that could hope to be seen by tuning friction factors. Simply by upgrading the bathymetry, especially in the Antarctic ice shelves and in Hudson Bay, the entirety of the globe shows dramatic improvement. Another very interesting result can be seen by comparing the Atlantic basin in both Figure 13c and 13e. In the global baseline, the entirety of the Atlantic is underpredicted. This is primarily due to too high of C_{it} for that basin. By using basin-sector-specific values, and by carefully choosing those values, the entire Atlantic ocean can be drastically improved. The improvement is not limited strictly to amplitudes either as 13d and 13f highlight. The complex error, which accounts for both amplitude and phase, also shows marked improvement between these two runs.

The improvement from the global optimization (13e and 13f) to the local re-optimization (13g and 13h) is more subtle. In this step, several areas were further sub-divided in order to provide more degrees of freedom to optimize local areas. Among these were dividing the European Shelf into the Irish Sea, English Channel, and the remainder of the European Shelf. By performing the re-optimization, results on the European Shelf were significantly improved. Another regions this procedure was used was in the Yellow and East China Seas. These two regions were further divided into the Sea of Japan, Korean Strait, Yellow Sea, and South China Sea. Again, this procedure greatly improved local solutions.

A final measure of model skill to consider is calculating the total tidal dissipation within the model. While there is a certain amount of uncertainty in what distribution of tidal dissipation exists in nature, it is relatively well accepted that tides dissipate approximately 3.6 terrawatts of energy (Munk, 1997). This value is calculated from astronomical inputs and thus has relative certainty. What is more unclear is the distribution between internal tide dissipation and boundary layer dissipation. Munk (1997) estimates 2.6 TW of dissipation on the shelves and 0.9 TW dissipated through internal tides. In our Global Baseline model, boundary layer dissipation accounted for 1.72 TW of dissipation and internal tides accounted for 1.49 TW. This brings the total dissipation to 3.21 TW, which is slightly lower than the accepted total. After performing the global and local optimizations, however, the new totals came out to 1.83 TW of boundary layer dissipation and 1.49 TW of internal tide dissipation. This brings the total dissipation to 3.31 TW in the local re-optimization. Note that we are missing lateral viscous dissipation which likely plays a roll in the high energy dissipation regions. Our findings indicate that more dissipation occurs due to internal wave conversion than was previously expected. Egbert and Ray (2001) estimate that 1 TW or more could be dissipated in the deep ocean (where dissipation is dominated by internal tides). Furthermore Green and Nycander (2013) raises this estimate even further, estimating that up to 1.18 TW are dissipated by internal tides. Our new findings seems to indicate that it could be higher than that by 50% or more. This is partly due to better attribution of dissipation as we directly compute it from the dissipation terms. Furthermore we better resolve both shelf regions and steep topography where internal dissipation dominates than previous data assimilated models, likely increasing internal tide dissipation along mid-oceanic ridges and shelf breaks.

Figure 14 shows the amplitude and phase of the M_2, Q_1, O_1, P_1, K_1, N_2, S_2, and K_2 tides. Additionally, Figure 15 shows the same constituents compared to global tidal stations.

Overall our optimized solution finds solutions with very low error metrics compared to both TPXO9 as well as tidal station data. Certainly bathymetric is a few select location plays a large role in tidal fidelity. Boundary layer dissipation is also critical in a few very limited regions. In fact 50% of the total global tidal boundary layer dissipation occurs over only 0.2% of the ocean. Furthermore, optimal bottom friction parameters align very well with the energetics of the very limited high dissipation regions. The large
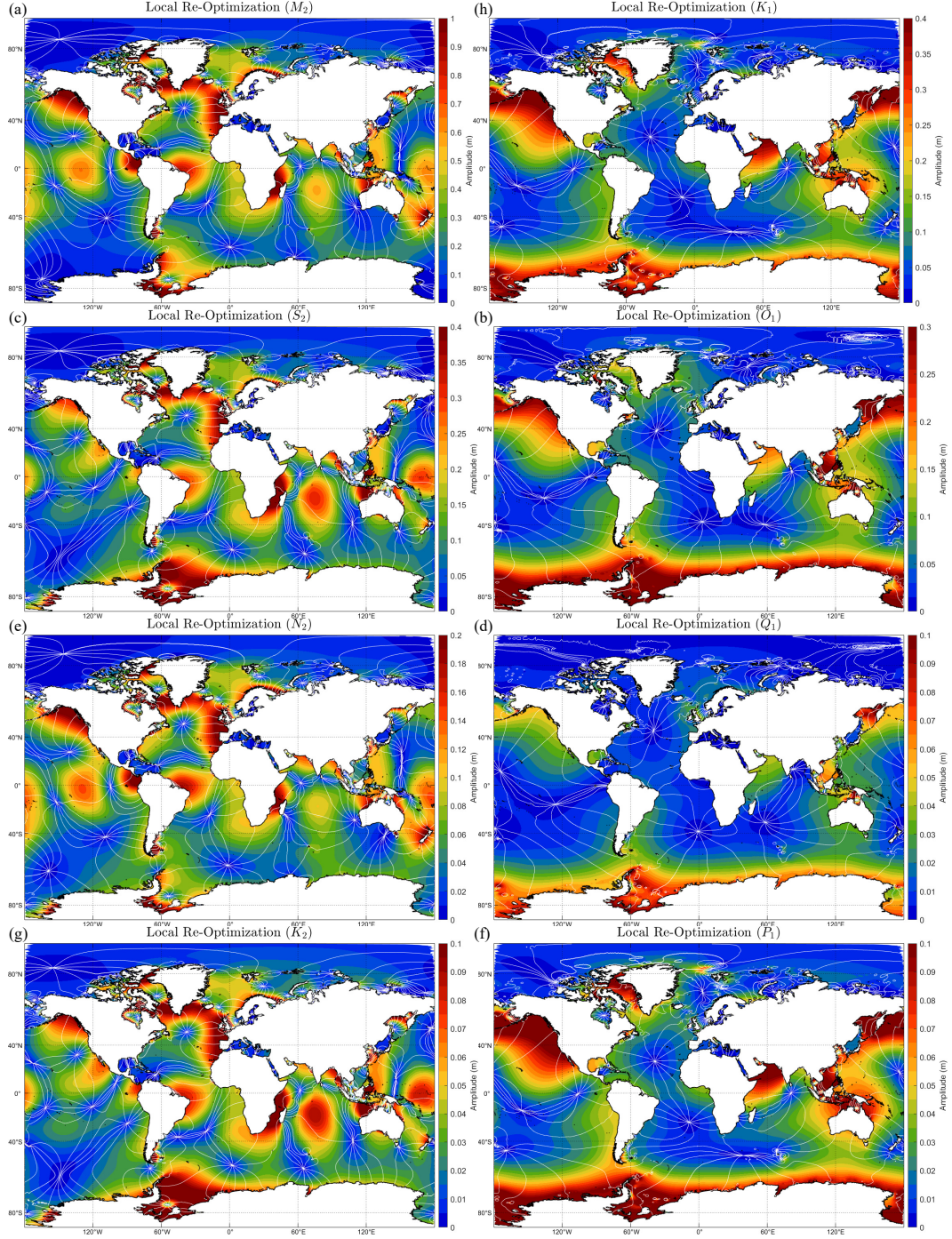
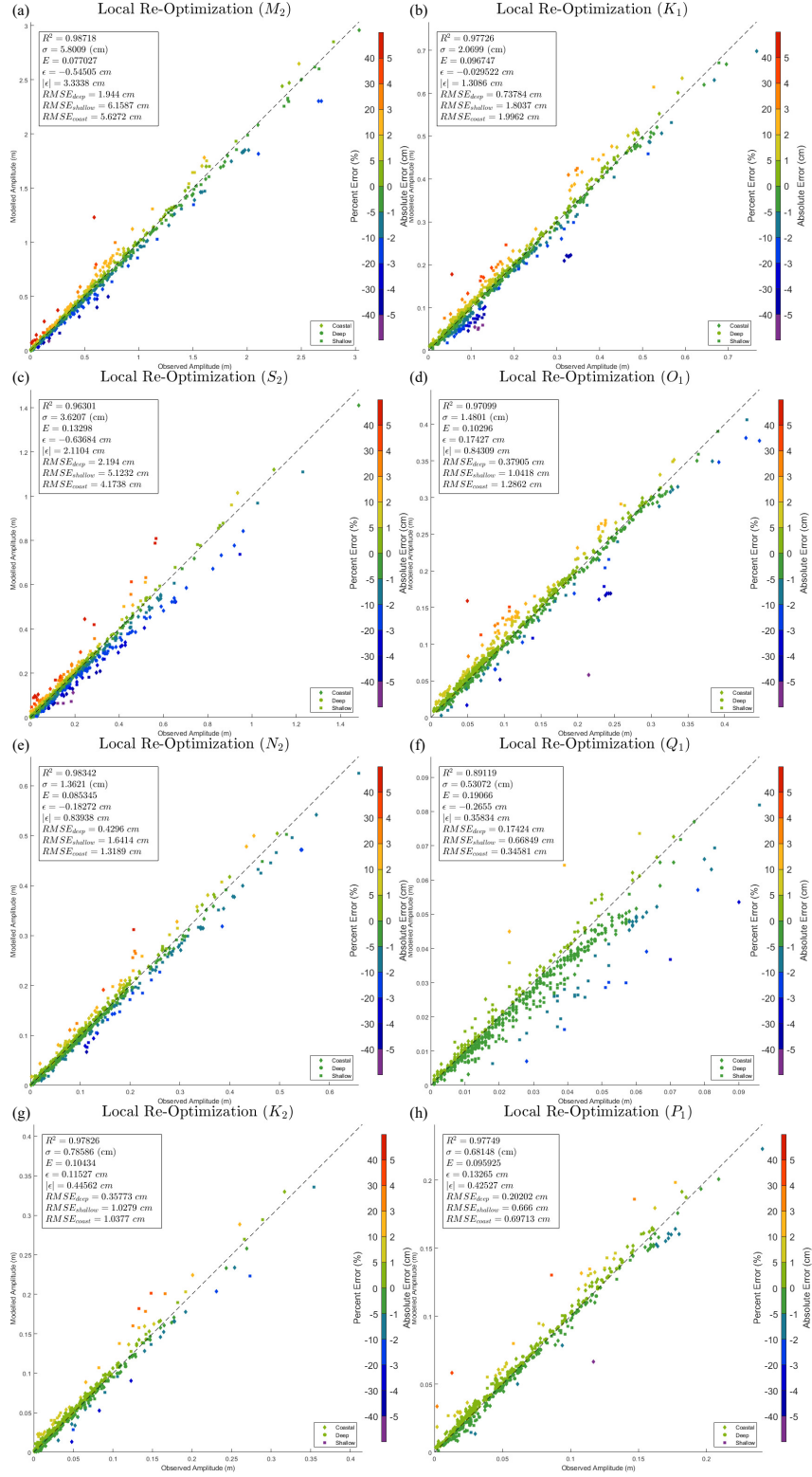**Figure 14.** Amplitude and phase of best solution.

Figure 15. Errors compared to tidal gauges of the best solution. Colorbars have the same error brackets as amplitude errors in Figure 13.

bottom friction values in the Arctic also make good physical sense. Especially interesting is investigating why dissipation parameterization coefficients are so high in the Aleutians and Ryukyu Islands. The missing lateral viscous dissipation due to highly energetic eddying is likely driving these high coefficients.

Certainly the sensitivity of the Ronne ice shelf needs to be explored in more detail. As we have suggested, there appears to be a resonant effect running North-South through the Atlantic. Further examination of this effect could be highly instructive and further the understanding of global tidal dynamics.

Another future course of action is to incorporate time varying salinity and temperature profiles from a high resolution global ocean model to drive ADCIRC's baroclinic pressure gradient terms. While this coupling has been performed on a regional mesh by using data from a global forecast system, it has not been studied on a global mesh (Pringle et al., 2019; Metzger et al., 2017). Incorporating this data will allow for live calculation of baroclinic currents, allowing for far better capture of currents systems in the ocean such as the Gulf Stream. By incorporating these currents, both the draw down and piling up of water along coasts due to such currents can be captured. Using live baroclinic information will also allow us to capture the seasonality of internal tide dissipation, which is known to vary throughout the year due to changing density and buoyancy. Finally, this information will allow for steric effects to be incorporated through post processing by estimating steric effects at various times during simulations.

Finally, while the optimization strategy used in this study was relatively rudimentary, it demonstrates that such techniques can result in large improvements in global tides. Further improvement of optimization techniques for this purpose could result in even greater improvement in tidal results.

Acknowledgments

References

Arbic, B. K., Karsten, R. H., & Garrett, C. (2009). On tidal resonance in the global ocean and the back-effect of coastal tides upon open-ocean tides. *Atmosphere-Ocean*, *47*(4), 239-266. doi: 10.3137/OC311.2009

Arcement, G. J., & Schneider, V. R. (1989). *Guide for selecting Manning's roughness coefficients for natural channels and flood plains* (- ed.; Tech. Rep.). doi: 10.3133/wsp2339

Atkinson, J. H., Roberts, H., Hagen, S., Zou, S., Bacopoulos, P., Medeiros, S., . . . Cobell, Z. (2011). Deriving Frictional Parameters and Performing Historical Validation for an ADCIRC Storm Surge Model of the Florida Gulf Coast. *Florida Watershed Journal*, *4*.

Atkinson, J. H., Westerink, J. J., & Hervouet, J. M. (2004a). Similarities between the quasi-bubble and the generalized wave continuity equation solutions to the shallow water equations. *Int. J. Numer. Meth. Fluids*, *45*(7), 689–714. doi: 10.1002/fld.700

Atkinson, J. H., Westerink, J. J., & Luettich Jr, R. A. (2004b). Two-dimensional dispersion analyses of finite element approximations to the shallow water equations. *Int. J. Numer. Meth. Fluids*, *45*(7), 715–749. doi: 10.1002/fld.701

Beaman, R. (2018). *High-resolution depth model for the northern australia – 100 m.*

Blakely, C. (2021). *Data Supporting Dissipation and Bathymetric Sensitivities in an Unstructured Mesh Global Tidal Model.* doi: https://doi.org/10.5281/zenodo.5563024

Boyer, T. P., Antonov, J. I., Baranova, O. K., Garcia, H. E., Johnson, D. R., Mishonov, A. V., . . . Levitus, S. (2013). *World ocean database 2013.* doi: http://doi.org/10.7289/V5NZ85MT

Bunya, S., Dietrich, J. C., Westerink, J. J., Ebersole, B. A., Smith, J. M., Atkinson, J. H., . . . Roberts, H. J. (2010). A High-Resolution Coupled Riverine Flow, Tide, Wind, Wind Wave, and Storm Surge Model for Southern Louisiana and Mississippi. Part I: Model Development and Validation. *Monthly Weather Review*, *138*(2), 345–377. Retrieved from https://journals.ametsoc.org/view/journals/mwre/138/2/2009mwr2906.1.xml doi: 10.1175/2009MWR2906.1

Chow, V. T. (1959). *Open-channel hydraulics.* New York : McGraw-Hill.

CHS, C. H. S. (2018). *Canadian Hydrographic Service Non-Navigational (NONNA) Bathymetric Data* [data set]. Retrieved from https://open.canada.ca/data/en/dataset/d3881c4c-650d-4070-bf9b-1e00aabf0a1d

Dietrich, J. C., Westerink, J. J., Kennedy, A. B., Smith, J. M., Jensen, R. E., Zijlema, M., . . . Cobell, Z. (2011). Hurricane Gustav (2008) Waves and Storm Surge: Hindcast, Synoptic Analysis, and Validation in Southern Louisiana. *Monthly Weather Review*, *139*(8), 2488–2522. Retrieved from https://journals.ametsoc.org/view/journals/mwre/139/8/2011mwr3611.1.xml doi: 10.1175/2011MWR3611.1

Dresback, K. M., Kolar, R. L., & Luettich, R. A., Jr. (2006). On the form of the momentum equation and lateral stress closure law in shallow water modeling. In *Estuarine and coastal modeling (2005)* (pp. 399–418).

Egbert, G. D., & Erofeeva, S. Y. (2002). Efficient inverse modeling of barotropic ocean tides. *Journal of Atmospheric and Oceanic Technology*, *19*(2), 183 - 204. Retrieved from https://journals.ametsoc.org/view/journals/atot/19/2/1520-0426_2002_019_0183_eimobo_2_0_co_2.xml doi: 10.1175/1520-0426(2002)019⟨0183:EIMOBO⟩2.0.CO;2

Egbert, G. D., & Erofeeva, S. Y. (2021). *TPXO9-Atlas* [data set]. Retrieved from https://www.tpxo.net/global/tpxo9-atlas

Egbert, G. D., & Ray, R. D. (2000). Significant dissipation of tidal energy in the deep ocean inferred from satellite altimeter data. *Nature*, *405*(6788),

775–778. Retrieved from https://doi.org/10.1038/35015531 doi: 10.1038/35015531

Egbert, G. D., & Ray, R. D. (2001). Estimates of M2 tidal energy dissipation from TOPEX/Poseidon altimeter data. *Journal of Geophysical Research: Oceans*, *106*(C10), 22475–22502. doi: https://doi.org/10.1029/2000JC000699

Garrett, C., & Kunze, E. (2007). Internal tide generation in the deep ocean. *Annual review of fluid mechanics*, *39*(1), 57–87.

GEBCO, B. C. G. (2014). *The GEBCO_2014 Grid, version 20150318* [data set]. Retrieved from https://www.bodc.ac.uk/data/open_download/gebco/GEBCO_30SEC/zip/

GEBCO, B. C. G. (2019). *The GEBCO_2019 Grid - a continuous terrain model of the global oceans and land.* [data set]. doi: 10.5285/836f016a-33be-6ddc-e053-6c86abc0788e

GEBCO, B. C. G. (2020). *The GEBCO_2020 Grid - a continuous terrain model of the global oceans and land.* [data set]. doi: 10.5285/a29c5465-b138-234d-e053-6c86abc040b9

Graham, L., Butler, T., Walsh, S., Dawson, C., & Westerink, J. J. (2017). A measure-theoretic algorithm for estimating bottom friction in a coastal inlet: Case study of bay st. louis during hurricane gustav (2008). *Monthly Weather Review*, *145*(3), 929 - 954. Retrieved from https://journals.ametsoc.org/view/journals/mwre/145/3/mwr-d-16-0149.1.xml doi: 10.1175/MWR-D-16-0149.1

Green, J. A. M., & Nycander, J. (2013). A comparison of tidal conversion parameterizations for tidal models. *Journal of Physical Oceanography*, *43*(1), 104–119. doi: 10.1175/JPO-D-12-023.1

Harris, P. T., Macmillan-Lawler, M., Rupp, J., & Baker, E. K. (2014). Geomorphology of the oceans. *Marine Geology*, *352*, 4–24. doi: https://doi.org/10.1016/j.margeo.2014.01.011

Hope, M., Westerink, J. J., Kennedy, A. B., Kerr, P., Dietrich, J., Dawson, C., ... Westerink, L. G. (2013). Hindcast and validation of Hurricane Ike (2008) waves, forerunner, and storm surge. *Journal of Geophysical Research*, *118*, 4424–4460. doi: 10.1002/jgrc.20314

Jeffreys, H. (1921). Tidal Friction in Shallow Seas. *Philosophical Transactions of the Royal Society of London. Series A, Containing Papers of a Mathematical or Physical Character*, *221*, 239–264.

Kennedy, A. B., Gravois, U., Zachry, B. C., Westerink, J. J., Hope, M. E., Dietrich, J. C., ... Dean, R. G. (2011). Origin of the Hurricane Ike forerunner surge. *Geophysical Research Letters*, *38*(8). doi: https://doi.org/10.1029/2011GL047090

Kerr, P. C., Martyr, R. C., Donahue, A. S., Hope, M. E., Westerink, J. J., Luettich Jr., R. A., ... Westerink, H. J. (2013). U.S. IOOS coastal and ocean modeling testbed: Evaluation of tide, wave, and hurricane surge response sensitivities to mesh resolution and friction in the Gulf of Mexico. *Journal of Geophysical Research: Oceans*, *118*(9), 4633–4661. doi: https://doi.org/10.1002/jgrc.20305

Luettich, R., & Westerink, J. (2004). *Formulation and Numerical Implementation of the 2D/3D ADCIRC Finite Element Model Version 44.XX* (Tech. Rep.). Retrieved from https://adcirc.org/wp-content/uploads/sites/2255/2018/11/adcirc_theory_2004_12_08.pdf

Lyard, F., Allain, D. J., Cancet, M., Carrère, L., & Picot, N. (2021). Fes2014 global ocean tide atlas: design and performance. *Ocean Science*, *17*(3), 615–649. Retrieved from https://os.copernicus.org/articles/17/615/2021/ doi: 10.5194/os-17-615-2021

Lyard, F., Lefevre, F., Letellier, T., & Francis, O. (2006). Modelling the global ocean tides: modern insights from FES2004. *Ocean Dynamics*, *56*(5), 394–415. doi: 10.1007/s10236-006-0086-x

MATLAB. (2018). *9.7.0.1190202 (r2019b)* [Computer Software]. Natick, Massachusetts: The MathWorks Inc.

Metzger, J. E., Helber, R. W., Hogan, P. J., Poset, P. G., Thoppil, P. G., Townsend, T. L., & Wallcraft, A. J. (2017). *Global ocean forecast system 3.1 validation testing* (Tech. Rep.). Naval Research Laboratory.

Munk, W. (1997). Once again: once again—tidal friction. *Progress in Oceanography*, *40*(1), 7–35. doi: https://doi.org/10.1016/S0079-6611(97)00021-9

Munk, W., & Wunsch, C. (1998). Abyssal recipes II: energetics of tidal and wind mixing. *Deep Sea Research Part I: Oceanographic Research Papers*, *45*(12), 1977–2010. Retrieved from https://www.sciencedirect.com/science/article/pii/S0967063798000703 doi: https://doi.org/10.1016/S0967-0637(98)00070-3

Pringle, W. J. (2017). *Global Tide Gauge Database* [dataset]. Retrieved from https://www.google.com/maps/d/u/0/viewer?mid=1yvnYoLUFS9kcB5LnJEdyxk2qz6g&ll=-3.81666561775622e-14\%2C101.96502786483464&z=2

Pringle, W. J., Gonzalez-Lopez, J., Joyce, B. R., Westerink, J. J., & van der Westhuysen, A. J. (2019). Baroclinic coupling improves depth-integrated modeling of coastal sea level variations around puerto rico and the u.s. virgin islands. *Journal of Geophysical Research: Oceans*, *124*(3), 2196-2217. doi: https://doi.org/10.1029/2018JC014682

Pringle, W. J., Wirasaet, D., Roberts, K. J., & Westerink, J. J. (2021). Global storm tide modeling with ADCIRC v55: unstructured mesh design and performance. *Geosci. Model Dev.*, *14*(2), 1125–1145. doi: 10.5194/gmd-14-1125-2021

Pringle, W. J., Wirasaet, D., Suhardjo, A., Meixner, J., Westerink, J. J., Kennedy, A. B., & Nong, S. (2018a). Finite-Element barotropic model for the Indian and Western Pacific Oceans: Tidal model-data comparisons and sensitivities. *Ocean Modelling*, *129*, 13–38. doi: 10.1016/j.ocemod.2018.07.003

Qian, S., Wang, D., Zhang, J., & Li, C. (2021). Adjoint estimation and interpretation of spatially varying bottom friction coefficients of the m2 tide for a tidal model in the bohai, yellow and east china seas with multi-mission satellite observations. *Ocean Modelling*, *161*, 101783. Retrieved from https://www.sciencedirect.com/science/article/pii/S1463500321000330 doi: https://doi.org/10.1016/j.ocemod.2021.101783

Roberts, K. J., & Pringle, W. J. (2018). *Oceanmesh2d: User guide - precise distance-based two-dimensional automated mesh generation toolbox intended for coastal ocean/shallow water* (Tech. Rep.). doi: https://doi.org/10.13140/RG.2.2.21840.61446/2

Roberts, K. J., Pringle, W. J., & Westerink, J. J. (2019a). OceanMesh2D 1.0: MATLAB-based software for two-dimensional unstructured mesh generation in coastal ocean modeling. *Geosci. Model Dev.*, *12*(5), 1847–1868. doi: 10.5194/gmd-12-1847-2019

Roberts, K. J., Pringle, W. J., Westerink, J. J., Contreras, M. T., & Wirasaet, D. (2019b). On the automatic and a priori design of unstructured mesh resolution for coastal ocean circulation models. *Ocean Modelling*, *144*, 101509. doi: https://doi.org/10.1016/j.ocemod.2019.101509

Schaffer, J., Timmermann, R., Arndt, J. E., Rosier, S. H. R., Anker, P. G. D., Callard, S. L., ... Roberts, D. H. (2019). *An update to Greenland and Antarctic ice sheet topography, cavity geometry, and global bathymetry (RTopo-2.0.4)* [data set]. PANGAEA. (Supplement to: Schaffer, Janin; Kanzow, Torsten; von Appen, Wilken-Jon; von Albedyll, Luisa; Arndt, Jan Erik; Roberts, David H (2020): Bathymetry constrains ocean heat supply to Greenland's largest glacier tongue. Nature Geoscience, 13(3), 227-231, https://doi.org/10.1038/s41561-019-0529-x) doi: 10.1594/PANGAEA.905295

Smagorinsky, J. (1963). General Circulation Experiments with the Primitive Equations: I. the Basic Experiment. *Monthly Weather Review*, *91*(3), 99–164. doi: 10.1175/1520-0493(1963)091⟨0099:GCEWTP⟩2.3.CO;2

Stammer, D., Ray, R. D., Andersen, O. B., Arbic, B. K., Bosch, W., Carrère, L., . . . Yi, Y. (2014). Accuracy assessment of global barotropic ocean tide models. *Reviews of Geophysics*, *52*(3), 243–282. doi: https://doi.org/10.1002/2014RG000450

Tanaka, S., Bunya, S., Westerink, J., Dawson, C., & Luettich Jr, R. (2010). Scalability of an Unstructured Grid Continuous Galerkin Based Hurricane Storm Surge Model. *Journal of Scientific Computing*, *46*, 329–358. doi: 10.1007/s10915-010-9402-1

Taylor, G. I., & Shaw, W. N. (1920). I. Tidal friction in the Irish Sea. *Philosophical Transactions of the Royal Society of London. Series A, Containing Papers of a Mathematical or Physical Character*, *220*(571-581), 1–33. doi: 10.1098/rsta.1920.0001

Wang, D., Zhang, J., & Wang, Y. P. (2021). Estimation of bottom friction coefficient in multi-constituent tidal models using the adjoint method: Temporal variations and spatial distributions. *Journal of Geophysical Research: Oceans*, *126*(5), e2020JC016949. Retrieved from `https://agupubs.onlinelibrary.wiley.com/doi/abs/10.1029/2020JC016949` (e2020JC016949 2020JC016949) doi: https://doi.org/10.1029/2020JC016949

Wang, X., Chao, Y., Shum, C., Yi, Y., & Fok, H. S. (2012). Comparison of Two Methods to Assess Ocean Tide Models. *Journal of Atmospheric and Oceanic Technology*, *29*(8), 1159–1167. doi: https://doi.org/10.1175/JTECH-D-11-00166.1

Wang, X., Verlaan, M., Apecechea, M. I., & Lin, H. X. (2021). Computation-Efficient Parameter Estimation for a High-Resolution Global Tide and Surge Model. *Journal of Geophysical Research: Oceans*, *126*(3), e2020JC016917. doi: https://doi.org/10.1029/2020JC016917

Westerink, J., Luettich, R., Feyen, J. C., Atkinson, J. H., Dawson, C., Roberts, H. J., . . . Pourtaheri, H. (2008). A basin- to channel-scale unstructured grid hurricane storm surge model applied to southern louisiana. *Monthly weather review*, *136*(3), 833–864.

Westerink, J., Luettich, R., Jr, Blain, C., & Scheffner, N. (1994). *Adcirc: An advanced three-dimensional circulation model for shelves, coasts, and estuaries. report 2. user's manual for adcirc-2ddi* (Tech. Rep.).